Numerical analysis of time-dependent conduit magma flow in dome-forming eruptions with application to Mount St. Helens 2004-2008

Ying-Qi Wong [1], and Paul Segall [1]

[1]Department of Geophysics, Stanford University, Stanford, CA, USA

Key Points:

- Magma flow regime abruptly transitions from viscous to plug flow throughout modeled eruptions
- Time-dependent and steady-state solutions agree for large chamber volume but differ for small chamber volume
- Time-dependent gas escape may explain the unique deformation time series at the only nearby continuous MSH GPS station

Corresponding author: Ying-Qi Wong, yqwong@stanford.edu

Abstract

Conduit models of volcanic eruptions simulate magma evolution through phase transitions and material changes during ascent. We present a time-dependent one-dimensional model of a chamber-conduit system to examine the temporal evolution of dome-forming eruptions. As magma ascends, volatiles exsolve and may escape vertically through the column or laterally through the conduit walls. Magma solidifies which increases viscosity, leading to a natural transition from viscous flow at depth to frictional sliding along the conduit walls near the surface, resulting in the extrusion of a semi-solid plug. The model evaluates time- and depth-dependent pressure, velocity, porosity and relative amounts of exsolved water to carbon dioxide. Transient effects arise when magma outflux from the chamber appreciably decreases pressure over the magma ascent timescale. For low magma permeability, transient effects increase porosity and velocity relative to steady-state solutions. For high magma permeability, efficient vertical and lateral gas escape depresses porosity and velocity at later times.

We use the model to predict three time-series datasets from the 2004-2008 eruption of Mount St. Helens: extruded volume, ground deformation and carbon dioxide emissions. We quantify sensitivity of model predictions to input parameters using the Distance-based Generalized Sensitivity Analysis. Chamber volatile content, volume and excess pressure influence the amplitude of observables, while conduit radius, frictional rate-dependence and magma permeability scale influence temporal evolution. High magma permeability can cause marked departures from exponentially decaying flux and may explain the unique temporal evolution of deformation observed at the only nearby continuous GPS station in operation at eruption onset.

1 Introduction

The increasing amount of data collected at volcanoes is driving advances in understanding the factors that control eruption type, duration and explosivity. Much of the data analysis focuses on inferences from individual data types, which range from ground deformation and seismic tomography to petrologic analyses and mapping of volcanic deposits. However, in recent years, significant efforts have been made to compare patterns in coeval datasets to build a more comprehensive view of magmatic systems, including tying ground deformation to eruption plume heights through changes in magma chamber pressure or volume (*Hreinsdóttir et al.* [2014] for Grimsvötn in Iceland and *Kozono et al.* [2014] for Shinmoe-dake in Japan), attributing correlated deformation, seismic amplitude and sulfur dioxide emission time series to changes in magma depth in the conduit (*Saballos et al.* [2014] for Concepción in Nicaragua), as well as linking tilt and seismic cycles through magma flow-induced shear stress (*Neuberg et al.* [2018] for Tungurahua in Ecuador).

Moving beyond empirical pattern recognition, physical models offer insight into processes governing magma ascent from a reservoir to the surface. These conduit flow models are based on fundamental conservation laws for simulating flow from chamber to surface, but are complicated by the effects of phase changes on magma properties such as density and viscosity which in turn regulate magma flux [e.g. *Gonnermann and Manga*, 2007]. Most conduit models focus on steady-state solutions [e.g. *Jaupart and Allègre*, 1991; *Papale*, 2001; *Mastin*, 2002; *Kozono and Koyaguchi*, 2009], which apply when magma ascent is fast and the chamber pressure is approximately constant over the eruption timescale. However, in slower eruptions, time-dependent models are needed to account for the feedback between flow, conduit properties and chamber pressure [*Melnik and Sparks*, 2006]. Time-dependent models have been developed to explain cyclic discharge in lava dome eruptions due to stick-slip motion of compressible Newtonian magma [*Denlinger and Hoblitt*, 1999] or through the build-up and release of frictional or viscous resistance [*De' Michieli Vitturi et al.*, 2013]. Other models attribute cyclic discharge to complex feedbacks

between magma velocity and crystallization kinetics or gas escape or both [*Melnik and Sparks*, 2005; *Kozono and Koyaguchi*, 2012].

In this study, we extend the 1D steady-state conduit flow model of *Wong et al.* [2017] to simulate time-dependent processes and estimate surface observables during dome-building eruptions. Magma ascending through a conduit exsolves volatiles and crystallizes, both of which strongly affect viscosity. Slower dome-building eruptions permit gases to escape, which, together with crystallization, is critical to forming dense, degassed plugs in the shallow reaches of conduits [e.g. *Schneider et al.*, 2012], an effect highly simplified in the earlier conduit model of *Anderson and Segall* [2011]. *Wong et al.* [2017] explicitly modeled gas escape using Darcy flow. Steady-state solutions were used to constrain chamber conditions and material properties (e.g. chamber pressure, total water content, magma permeability) during the quasi-steady extrusion phase of the Mount St. Helens 2004-2008 eruption. Nevertheless, typical chamber properties and extrusion flux in dome-forming eruptions imply that time-dependent processes cannot be neglected when simulating the whole eruption, thus we develop and verify a numerical model for time-dependent flow. We first compare time-dependent and steady-state solutions, then apply the model to the Mount St. Helens eruption using time-series data that includes ground deformation, extrusion flux and gas emission rates.

2 Physics-based flow model of magma chamber and conduit

The model comprises an ellipsoidal magma chamber connected by a conduit to the surface (Figure 1) [*Wong et al.*, 2017]. Properties in the chamber are taken as lumped parameters evolving with time, while properties in the conduit are modeled in both time and depth (radially-averaged). We first introduce the magma mixture model, then describe the governing equations followed by the gas escape model (symbols are given in Table 1).

2.1 Constitutive models for magma density and viscosity

Magma consists of solids, liquid melt, as well as dissolved and exsolved volatile components, giving its density as

$$\rho = \rho_s \phi_s + \rho_l \phi_l + \rho_h^d \phi_h^d + \rho_c^d \phi_c^d + \rho_h^e \phi_h^e + \rho_c^e \phi_c^e. \tag{1}$$

The subscripts s, l, h, c refer to solids, liquid melt, water (H_2O) and carbon dioxide (CO_2) respectively, while superscripts d, e indicate dissolved and exsolved volatile components. For each phase, the density and volume fraction are ρ and ϕ respectively. As in *Wong et al.* [2017], we derive the solid volume fraction ϕ_s by assuming isothermal equilibrium crystallization of the water-saturated Mount St. Helens dacite [*Schneider et al.*, 2012; *Pallister et al.*, 2008]. For simplicity, we assume that crystals are anhydrous: volatiles in the system are either dissolved in the liquid ($\rho_h^d \phi_h^d + \rho_c^d \phi_c^d$) or in the gas phase ($\rho_h^e \phi_h^e + \rho_c^e \phi_c^e$).

Measurements of dissolved volatile components from petrology are usually expressed as mass concentrations (χ_h^d, χ_c^d), not volume fraction, thus we relate these two variables using

$$\chi_h^d = \frac{\rho_h^d \phi_h^d}{\rho_l \phi_l + \rho_h^d \phi_h^d + \rho_c^d \phi_c^d}, \quad \chi_c^d = \frac{\rho_c^d \phi_c^d}{\rho_l \phi_l + \rho_h^d \phi_h^d + \rho_c^d \phi_c^d}. \tag{2}$$

Rearranging, we obtain the component density of each dissolved volatile species,

$$\rho_h^d \phi_h^d = \chi_h^d \rho_l \phi_l c_1, \quad \rho_c^d \phi_c^d = \chi_c^d \rho_l \phi_l c_1, \tag{3}$$

where

$$c_1 = \frac{1}{1 - \chi_h^d - \chi_c^d}. \tag{4}$$

We apply the solubility relations from *Liu et al.* [2005] to derive the mass concentrations of dissolved water and carbon dioxide χ_h^d and χ_c^d at a specified pressure and temperature.

92 **Table 1.** Symbols used in this study. Nominal values for the model parameters are given.

| Symbol	Description	Equation or Reference Value
Model parameters		
α	Magma chamber aspect ratio (width/height)	0.66
V_0	Magma chamber volume	100 km^3
Ω	Magma chamber recharge rate	0 m^3 day^{-1} Pa^{-1}
L	Conduit length	4 km
R	Conduit radius	50 m
f_0	Nominal coefficient of friction	0.1
a	Rate-dependence of friction	10^{-2}
k_c	Scaling parameter for magma permeability	10^{-13} m^2
ϕ_{gc}	Percolation threshold	0.3
Δp_0	Excess pressure at conduit base at $t = 0$	19 MPa
χ_h^{ch}	Total water content at conduit base	5 wt%
χ_c^{ch}	Total carbon dioxide content at conduit base	2000 ppm
Dependent variables solved in numerical solution		
p	Pressure	
v	Velocity	
ϕ_g	Gas volume fraction	
m_h	Mole fraction of exsolved H_2O	
Other dependent variables		
c_1	Relationship between volatile mass concentration and volume fraction	Equation 4
$k_{\mathrm{mag}}, k_{\mathrm{wall}}, k_{\mathrm{lat}}, k_{\mathrm{vert}}$	Permeabilities (magma, wall rock, lateral, vertical)	Equations 14, 15
m_c	Mole fraction of exsolved CO_2	$1 - m_h$
$p_{\mathrm{ch}}, p_{\mathrm{deep}}$	Chamber pressure, pressure in deep magma source	$p(z = -L, t)$, $p_{\mathrm{ch}}(t = 0)$
p_{hyd}	Pore pressure in the crust	$\rho_{\mathrm{hyd}} g z$
q	Mass flow rate at conduit base	ρv
u_g, v_g	Gas velocity (lateral, vertical)	Equation 13
$v_{\mathrm{visc}}, v_{\mathrm{fric}}$	Velocity (viscous, frictional)	Equation 8
$\beta_{\mathrm{ch}}, \beta_{\mathrm{mag}}$	Compressibility (chamber, magma)	Equation 19
$\dot{\gamma}$	Magma strain rate	$2v/R$
Γ	Ratio of mass concentrations of exsolved CO_2 to H_2O	Equation 5
η, η_m, η_s	Mixture viscosity, melt viscosity, relative viscosity due to solids	Equation 7
λ	Length scale for lateral gas escape	$2R$
ρ	Mixture magma density	Equation 1
ρ_g	Gas density	Ideal gas law
σ, σ_c	Normal stress (Lithostatic, effective)	$\rho_{\mathrm{lith}} g z$, $\sigma - p_{\mathrm{hyd}}$
τ_R	Shear stress along conduit wall	Equation 9
ϕ_s, ϕ_l	Volume fraction (solid, melt)	*Schneider et al.* [2012]
$\phi_h^d, \phi_c^d, \phi_h^e, \phi_c^e$	Volume fraction of dissolved H_2O & CO_2, exsolved H_2O & CO_2	Equations 3, 5
χ_h^d, χ_c^d	Mass concentration of dissolved H_2O & CO_2	Equation 2
$\chi_h^{e,ch}, \chi_c^{e,ch}$	Mass concentration of exsolved H_2O & CO_2 in chamber	Equations 20, 21
Prescribed parameters		
g	Gravitational acceleration	9.81 m s^{-2}
$k_{\mathrm{wall}}^{\mathrm{top}}$	Wall rock permeability at surface	10^{-14} m^2
$\mathcal{M}_h, \mathcal{M}_c$	Molar masses of H_2O & CO_2	18.02, 44.01 g mol^{-1}
p_{atm}	Atmospheric pressure	0.1 MPa
R_w, R_c	Gas constants for H_2O & CO_2	461.5, 188.9 J kg^{-1} K^{-1}
T	Temperature of magma	850 °C
v_r	Reference velocity for friction	10^{-5} m s^{-1}
η_g	Gas viscosity	10^{-4} Pa s
μ	Shear modulus of crust	20 GPa
$\rho_s, \rho_l, \rho_h^d, \rho_c^d$	Densities of solids, melt, dissolved H_2O & CO_2	2600, 2200, 2200, 2200 kg m^{-3}
$\rho_{\mathrm{hyd}}, \rho_{\mathrm{lith}}$	Density of water, host rock	1000, 2700 kg m^{-3}
Timescales used in analysis		
T_{asc}	Timescale of magma ascent	L/v
T_{ch}	Timescale of chamber pressure evolution	Equation 24
$T_{\mathrm{lat}}, T_{\mathrm{vert}}$	Timescale of lateral, vertical gas escape	R/u_g, $z_{\phi gc}/(v_g - v)$
T_{rat}	Ratio of chamber pressure evolution to magma ascent timescale	$T_{\mathrm{ch}}/T_{\mathrm{asc}}$
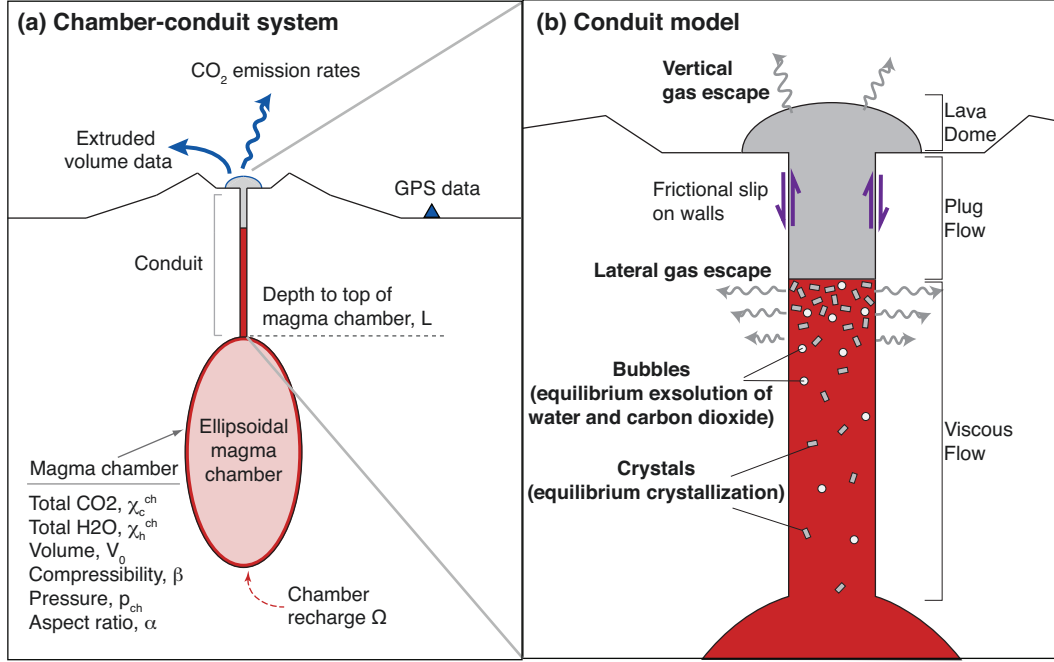
Figure 1. Model geometry and setup, adapted from *Wong et al.* [2017]. (a) Magma chamber and conduit geometry with surface observables. Properties of the magma chamber are taken as lumped parameters. (b) Details of the conduit model. Text in bold indicates additional processes considered compared with *Anderson and Segall* [2011]. At depth, magma flows viscously, however, at shallower depths, magma solidification, gas exsolution and escape cause flow to evolve to frictional sliding.

Note that the slightly different formulation of c_1 compared to *Wong et al.* [2017] is due to a modified definition of volatile mass concentration: here, the volatile mass fraction is taken relative to the melt plus dissolved volatile content, while in *Wong et al.* [2017] the volatile mass fraction is taken relative to the melt only. The difference between these two definitions is small for reasonable volatile mass fractions, however the current version is more accurate.

The gas phase comprises water and carbon dioxide vapor through their relative mass fractions,

$$\rho_h^e \phi_h^e = \frac{m_h \mathcal{M}_h}{m_h \mathcal{M}_h + m_c \mathcal{M}_c} \rho_g \phi_g = \frac{1}{1+\Gamma} \rho_g \phi_g,$$
$$\rho_c^e \phi_c^e = \frac{m_c \mathcal{M}_c}{m_h \mathcal{M}_h + m_c \mathcal{M}_c} \rho_g \phi_g = \frac{\Gamma}{1+\Gamma} \rho_g \phi_g,$$

(5)

where m_h is the mole fraction of water in the vapor phase, $m_c = 1 - m_h$ is the mole fraction of carbon dioxide in the vapor phase, while $\mathcal{M}_h, \mathcal{M}_c$ are the molar masses of water and carbon dioxide respectively. Additionally, ρ_g is the gas phase density obtained from the ideal gas law while ϕ_g is the gas volume fraction. For convenience, we define a parameter $\Gamma = m_c \mathcal{M}_c / m_h \mathcal{M}_h$, the mass ratio of exsolved carbon dioxide to water. The only volume fraction left to define is ϕ_l, which is given by the remaining magma volume fraction,

$$\phi_l = 1 - \phi_s - \phi_h^d - \phi_c^d - \phi_g.$$

(6)

Magma viscosity is affected by these component phases, and is a combination of the melt viscosity η_m and the relative viscosity increase due to solids η_s,

$$\eta = \eta_m(\chi_h^d, \chi_c^d, T) \, \eta_s(\phi_s, \dot{\gamma}), \tag{7}$$

We apply the dacite melt viscosity model of *Whittington et al.* [2009], which depends on dissolved volatile content and temperature. For the relative viscosity increase due to solids, we apply the model of *Costa* [2005] and *Caricchi et al.* [2007] which incorporates dependence on strain rate $\dot{\gamma}$. The effect of bubbles on viscosity is neglected since porosity of the 2005 Mount St. Helens dome lavas is relatively low, thus the effect of crystals predominates [*Llewellin and Manga*, 2005].

2.2 Governing equations

The governing equations for the 1D conduit consist of radially-averaged momentum balance and three continuity equations. As in *Wong et al.* [2017], we assume isothermal flow given that most eruptions are short relative to the timescale of conduction in rocks. In the viscous flow regime, momentum balance is described by the Navier-Stokes equation. We perform a scaling analysis to identify dominant terms and summarize the results here (details in Supplementary Information Section S1). In dome-forming eruptions, the small Mach number allows momentum balance to be modeled as incompressible, while small velocities and high viscosities cause inertial effects to become negligible. These conditions reduce the Navier-Stokes equation to incompressible, steady, laminar Poiseuille Flow. We additionally allow frictional slip on the conduit walls, following the regularized rate-dependent friction law of *Rice et al.* [2001] while assuming no state evolution effects for high temperature sliding of granite [*Blanpied et al.*, 1998]. Magma velocity is thus the sum of viscous and frictional components,

$$v = v_{\text{visc}} + v_{\text{fric}} = \frac{\tau_R R}{4\eta} + 2v_r \exp\left(-\frac{f_0}{a}\right) \sinh\left(\frac{\tau_R}{a\sigma_c}\right), \tag{8}$$

where τ_R is the shear stress along the conduit walls,

$$\tau_R = -\frac{R}{2}\left(\frac{\partial p}{\partial z} + \rho g\right). \tag{9}$$

The vertical pressure gradient is $\partial p/\partial z$ and gravitational acceleration is g. The conduit has constant radius R and the conduit walls have depth-dependent effective normal stress $\sigma_c(z)$, which is approximated as the difference between lithostatic normal stress and hydrostatic pore pressure, $(\rho_{\text{lith}} - \rho_{\text{hyd}})gz$, neglecting tectonic and topographic contributions. Wall friction is parametrized by the nominal coefficient f_0, rate-dependence a, and reference velocity v_r.

The momentum balance allows a natural change in flow regime from viscous flow at depth to frictional sliding close to the surface. Deep in the conduit, low magma viscosity ($\sim 10^5$ Pa s) and high normal stress on the conduit walls result in $v_{\text{visc}} \gg v_{\text{fric}}$ and the magma flows viscously. At shallower depths, higher magma viscosity ($\sim 10^{18}$ Pa s) and lower normal stress on the conduit walls cause v_{fric} to dominate so that magma slides along the conduit walls as a solid plug. We therefore adopt a mechanical definition for the plug, which is formed when $v_{\text{fric}} \geq v_{\text{visc}}$.

The continuity equations for solids and liquids, water, and carbon dioxide respectively are given by

$$\frac{\partial}{\partial t}(\rho_s \phi_s + \rho_l \phi_l) = -\frac{\partial}{\partial z}[(\rho_s \phi_s + \rho_l \phi_l)v] \tag{10}$$

$$\frac{\partial}{\partial t}\left(\chi_h^d \rho_l \phi_l c_1 + \frac{1}{1+\Gamma}\rho_g \phi_g\right) = -\frac{\partial}{\partial z}\left[\left(\chi_h^d \rho_l \phi_l c_1 + \frac{1}{1+\Gamma}\rho_g \phi_g\right)v + \frac{1}{1+\Gamma}\rho_g \phi_g(v_g - v)\right] - \frac{2\rho_g \phi_g u_g}{R(1+\Gamma)} \tag{11}$$

$$\frac{\partial}{\partial t}\left(\chi_c^d \rho_l \phi_l c_1 + \frac{\Gamma}{1+\Gamma}\rho_g \phi_g\right) = -\frac{\partial}{\partial z}\left[\left(\chi_c^d \rho_l \phi_l c_1 + \frac{\Gamma}{1+\Gamma}\rho_g \phi_g\right)v + \frac{\Gamma}{1+\Gamma}\rho_g \phi_g(v_g - v)\right] - \frac{2\Gamma\rho_g \phi_g u_g}{R(1+\Gamma)}, \tag{12}$$

[e.g. *Wong et al.*, 2017; *Schneider et al.*, 2012; *Kozono and Koyaguchi*, 2012]. As magma ascends, solids forming from the melt cause the solid mass fraction to increase and the melt mass fraction to decrease (equation 10). Volatile components in the solids are neglected for simplicity, thus there is no sink term on the right side of equation 10 and permits separation of solids from the volatile continuity equations. In equations 11 and 12, the first term on the right side is the flux of dissolved and exsolved volatiles. The second and third terms on the right represent vertical and lateral gas flow out of the conduit at gas velocities v_g and u_g respectively [e.g. *Kozono and Koyaguchi*, 2012; *Schneider et al.*, 2012]. Details of the gas escape model is in the next section. At steady-state, the terms on the left-hand side, which represent time-dependent mass change of each component, are identically zero [*Wong et al.*, 2017]. In this study, we retain these transient terms which impact mass change and therefore momentum balance in the system.

2.3 Gas escape from the conduit

As in *Wong et al.* [2017], Darcy's Law is used to model gas loss while assuming chemical and mechanical equilibrium between the gas phase and the ambient melt, specifically that gas and melt pressures are the same [*Jaupart and Allègre*, 1991; *Schneider et al.*, 2012; *Kozono and Koyaguchi*, 2012]. Vertical gas flow is driven by the magma pressure gradient. Lateral gas escape is computed using a "membrane-diffusion" model, which approximates radial diffusion with that appropriate for flow across a thin permeable membrane bordering a fluid reservoir at hydrostatic pressure. Lateral gas flow is driven by the difference between magma pressure and the far-field hydrostatic pressure (p_{hyd}) over a length scale λ. Here we approximate that the damage zone around the conduit scales with radius R, giving $\lambda = 2R$. Vertical and lateral gas velocities are scaled by their respective permeabilities $k_{\text{vert}}, k_{\text{lat}}$ and are inversely proportional to the gas viscosity η_g,

$$(v_g - v) = \frac{k_{\text{vert}}}{\eta_g}\frac{\partial p}{\partial z}$$
$$u_g = \frac{k_{\text{lat}}}{\eta_g}\frac{p - p_{\text{hyd}}}{\lambda}. \tag{13}$$

In the above equations, we impose η_g, λ and $p_{\text{hyd}} = \rho_{\text{hyd}}gz$, while $p, \partial p/\partial z$ are part of the solution. This leaves the permeabilities $k_{\text{vert}}, k_{\text{lat}}$ to be defined. In vertical gas escape, gas flows through the magma only. Magma permeability follows the Carman-Kozeny relation,

$$k_{\text{mag}} = k_c \phi_g^3, \quad \phi_g > \phi_{gc}, \tag{14}$$

where k_c is a scaling constant and ϕ_{gc} is the percolation threshold, which is the minimum porosity to form interconnected pathways and has a typical value is 0.3 [*Klug and Cashman*, 1996; *Saar and Manga*, 1999; *Blower*, 2001]. Therefore $k_{\text{vert}} = k_{\text{mag}}$. In lateral gas escape, gas flows through both magma and the wall rock, thus we combine the magma permeability with an average crustal permeability model from *Manning and Ingebritsen* [1999],

$$\frac{\lambda}{k_{\text{lat}}} = \frac{R}{k_{\text{mag}}} + \frac{\lambda - R}{k_{\text{wall}}}. \tag{15}$$

The above treatment of gas escape and permeability is identical to that in *Wong et al.* [2017]. Similarly, there are two modifications to the permeability model to address permeability hysteresis and plug permeability. We retain these modifications although their numerical implementation differs.

First, permeability hysteresis preserves permeability in compacting magma despite porosity dropping below the percolation threshold [*Rust and Cashman*, 2004; *Colombier et al.*, 2017]. As a function of depth, we simulate this behavior by calculating permeability at depths above the percolation threshold following equation 14, even if porosity drops below the threshold. As a function of time, the percolation threshold depth is stored using persistent variables. At the next time step, the percolation threshold can either deepen or remain at the same depth depending on the updated porosity depth profile, but it may not ascend as the magma in that region is already permeable (more detail in Appendix A.1).

Second, we allow enhanced permeability to develop in the plug. In the semi-solid plug, magma viscosity is high which limits bubble expansion, even though depressurization decreases both solubility and the gas density. The relatively low dome rock porosity (5-10%) of the Mount St Helens hand samples [*Cashman et al.*, 2008; *Smith et al.*, 2011] implies that either gas overpressure develops, or gas escapes to maintain equilibrium with the surrounding magma. We assume the latter to occur through enhanced permeability at low melt fraction, such as through the formation of cracks, as described in *Wong et al.* [2017]. This requires modification of the appropriate continuity equations, a switch we refer to as "plug gas loss" (more detail in Appendix A.2).

Including these constitutive relations closes the system of equations and leaves four remaining field variables, compiled into the vector $y(z,t) = [p, v, \phi_g, m_h](z,t)$.

3 Numerical solution to governing equations

3.1 Discretization in depth

We semi-discretize the conduit domain in depth to transform the governing equations (equations 8, 10-12) into a system of first order differential equations in time of the form,

$$M(t,y)\frac{\partial y}{\partial t} = F\left(t, y, \frac{\partial y}{\partial z}\right), \tag{16}$$

where y contains solution elements $y(z,t) = [p, v, \phi_g, m_h](z,t)$. The mass matrix $M(t,y)$ contains partial derivatives of the component densities with respect to the field variables, e.g. $\partial(\rho_s \phi_s + \rho_l \phi_l)/\partial p$. Given the choice of constitutive relations, these component densities are independent of v, therefore the columns in the mass matrix corresponding to $\partial v/\partial t$ contain zeros. In addition, since inertial effects are neglected, the rows in the mass matrix corresponding to momentum balance contain zeros. The mass matrix is therefore singular, resulting in a first-order differential algebraic equation (DAE). The right hand side term F contains the remaining terms in the governing equations, including all the terms in the momentum balance equation as well as the flux and sink terms in the continuity equations.

We choose a staggered grid configuration in depth (Figure 2) [e.g. *de' Michieli Vitturi et al.*, 2010]. Cell centers for v (Grid 2) are offset from cell centers for p, ϕ_g, m_h (Grid 1) to allow strong coupling between velocity and pressure gradient, which helps to avoid convergence problems and spurious oscillations [*Ferziger and Peric*, 2002]. Using a finite volume framework, the governing equations are integrated over each depth cell, here

showing the continuity of solids and liquids as an example,

$$\int_{z_i^B}^{z_i^T} \frac{\partial}{\partial t}(\rho_s \phi_s + \rho_l \phi_l) dz + \int_{z_i^B}^{z_i^T} \frac{\partial}{\partial z}[(\rho_s \phi_s + \rho_l \phi_l)v] dz = 0$$

$$\frac{\partial}{\partial t}(\rho_s \phi_s + \rho_l \phi_l)\Delta z + (\rho_s \phi_s + \rho_l \phi_l)_i^T v_i - (\rho_s \phi_s + \rho_l \phi_l)_i^B v_{i-1} = 0. \qquad (17)$$
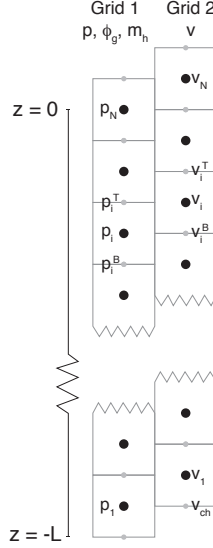

Figure 2. Spatial discretization of the conduit. The cell centers for velocity are offset by $0.5\Delta z$ from the cell centers for p, ϕ_g, m_h. Note that the model is radially averaged, thus the adjacent grids are for illustration purposes and do not indicate radial variations.

Superscripts T and B denote the top and bottom faces of cell i of Grid 1. The above result is equivalent to the finite difference approach, but emphasizes that solution components are average cell values and that discontinuities may exist between cells, for example at the percolation threshold and plug depth. Since p, ϕ_g, m_h determine phase volume fractions, $(\rho_s \phi_s + \rho_l \phi_l)_i$ is defined at the center of Grid 1. Interpolation to derive top and bottom cell face values is performed using Quadratic Upstream Interpolation for Convective Kinematics (QUICK), which is conducive for propagating information along the flow direction [*Leonard*, 1995]. Due to the staggered grid, velocities are conveniently defined at the Grid 1 cell faces (corresponding to v_{i-1}, v_i in Grid 2).

A similar derivation is applied to the momentum balance and volatile continuity equations. The pressure gradient is obtained using central finite difference at the Grid 1 cell faces, which coincide with cell centers of Grid 2 where velocity is defined. The volatile continuity equations additionally require gas velocities. Lateral gas velocity u_g is naturally defined at the Grid 1 cell center since it depends on p, ϕ_g. Vertical gas velocity v_g requires evaluation at the Grid 1 cell face: the pressure gradient is already defined there while porosity requires interpolation with QUICK. The discretized system is then advanced in time using MATLAB's `ode15s`, which is capable of handling time- and state-dependent mass matrices for a first-order DAE.

Rigorous verification of the code was executed using the Method of Manufactured Solutions (MMS) to ensure that the correct equations were being solved, without requiring a closed-form analytic solution [e.g. *Salari and Knupp*, 2000]. The method takes an

analytic expression (the "manufactured solution") that is smooth, at least second-order differentiable (since the second order derivative $\partial^2 p/\partial z^2$ arises from vertical gas escape) and that satisfies the true boundary conditions. First, the governing equations are evaluated analytically with the manufactured solution of the field variables and their respective derivatives at all depths and times. Since the manufactured solution is not the true solution, the governing equations will not be exactly satisfied, producing an analytic correction term. Next, the modified system with the analytic correction term is solved numerically. When the numerical method is implemented correctly, the numerical solution should equal the manufactured solution. This verification is repeated for different depth discretizations to ensure convergence that is consistent with the spatial discretization schemes. Details on the MMS implementation and convergence test are described in Supplementary Information Section S2.

3.2 Boundary conditions

The discretized governing system gives $4(N-1)$ equations in depth and requires 4 boundary conditions: conduit base pressure, total water and carbon dioxide contents, as well as surface pressure. The conduit base pressure evolves with the magma flux in and out of the magma chamber [e.g. *Segall*, 2013],

$$\frac{dp_{\text{ch}}}{dt} = \frac{q_{\text{in}} - q_{\text{out}}}{\rho_0 V_0 (\beta_{\text{mag}} + \beta_{\text{ch}})} = \frac{\Omega(p_{\text{deep}} - p_{\text{ch}}) - \pi R^2 v_{\text{ch}}}{V_0 (\beta_{\text{mag}} + \beta_{\text{ch}})}, \tag{18}$$

where Ω is a proportionality constant linking recharge in the chamber to the magmastatic head between the chamber and a deep reservoir at pressure p_{deep}, v_{ch} is the velocity at the conduit base, V_0 is the initial chamber volume, while β_{mag} and β_{ch} are the magma and chamber compressibilities respectively,

$$\beta_{\text{mag}} = \frac{1}{\rho}\frac{\partial\rho}{\partial p}, \quad \beta_{\text{ch}} = \frac{1}{V}\frac{\partial V}{\partial p}, \tag{19}$$

where ρ, p are evaluated at the center of the chamber [*Anderson and Segall*, 2011]. Magma density in the chamber is calculated using equation 1, while chamber center pressure is the sum of pressure at the conduit inlet and magmastatic from the chamber top to center. Chamber compressibility is estimated from the numerical results for different ellipsoidal chamber shapes following *Amoruso and Crescentini* [2009].

Total water and carbon dioxide concentrations, χ_h^{ch}, χ_c^{ch} are used to derive ϕ_g^{ch} and m_h^{ch}, the porosity and mole fraction of water at the conduit base. First the dissolved mass concentration of each volatile species χ_c^d, χ_h^d is determined from the solubility relations [*Liu et al.*, 2005] as functions of pressure, temperature and mole fraction of water. The dissolved concentrations are then subtracted from the total concentrations to find the exsolved mass concentrations $\chi_h^{e,ch}, \chi_c^{e,ch}$ to give m_h^{ch} implicitly,

$$\Gamma^{ch} = \frac{(1 - m_h^{ch})\mathcal{M}_c}{m_h^{ch}\mathcal{M}_h} = \frac{\chi_c^{e,ch}}{\chi_h^{e,ch}} = \frac{\chi_c^{ch} - \chi_c^d(p_{ch}, T, m_h^{ch})}{\chi_h^{ch} - \chi_h^d(p_{ch}, T, m_h^{ch})}. \tag{20}$$

The exsolved mass concentrations then give the gas volume fraction in the chamber ϕ_g^{ch},

$$\chi_h^{e,ch} + \chi_c^{e,ch} = \left[\frac{\rho_g \phi_g}{\rho_l \phi_l c_1}\right]^{ch}. \tag{21}$$

In this study, χ_h^{ch}, χ_c^{ch} were constant in time, however these inputs can be modified to accommodate time-varying volatile influx.

Finally, the surface pressure is assumed to be atmospheric pressure.

3.3 Scaling analysis of conduit base pressure boundary condition: the steady-state limit

The timescale of magma ascent relative to chamber pressure evolution (equation 18) determines the importance of the transient terms in the continuity equations. We perform a scaling analysis to identify cases where the steady-state limit is a valid approximation to the governing equations. For example, scaling the continuity of solids and liquids at $t = 0$,

$$\frac{1}{T_{\text{trans}}} \frac{\partial}{\partial t^*}(\rho_s \phi_s + \rho_l \phi_l) + \frac{v_{\text{ch}}^0}{L} \frac{\partial}{\partial z^*}[(\rho_s \phi_s + \rho_l \phi_l)v^*] = 0. \tag{22}$$

Variables with an asterisk are non-dimensional, v_{ch}^0 is the initial velocity of magma exiting the chamber and L is the conduit length. In the steady-state limit, the transient term timescale T_{trans} should be large relative to the ascent timescale $L/v_{\text{ch}}^0 = T_{\text{asc}}$ to make the transient term vanishingly small. The transient term timescale is controlled by the chamber pressure evolution, and can be derived by non-dimensionalizing the variables in Equation 18 assuming that $p_{\text{deep}} = p_{\text{ch}}(t = 0) = p_{\text{ch}}^0$,

$$\frac{1}{T_{\text{ch}}} \frac{dp_{\text{ch}}^*}{dt^*} = \frac{\Omega}{V_0(\beta_{\text{mag}} + \beta_{\text{ch}})}(1 - p_{\text{ch}}^*) - \frac{\pi R^2 v_{\text{ch}}^0}{p_{\text{ch}}^0 V_0(\beta_{\text{mag}} + \beta_{\text{ch}})} v_{\text{ch}}^*. \tag{23}$$

This gives two possible timescales for chamber evolution depending on the rate of recharge Ω,

$$T_{\text{ch}}^{(1)} = \frac{V_0(\beta_{\text{mag}} + \beta_{\text{ch}})}{\Omega} \qquad \text{(fast recharge)},$$

$$\text{or } T_{\text{ch}}^{(2)} = \frac{p_{\text{ch}}^0 V_0(\beta_{\text{mag}} + \beta_{\text{ch}})}{\pi R^2 v_{\text{ch}}^0} \qquad \text{(slow recharge)}. \tag{24}$$

With sufficiently large chamber volume and/or compressibility, $T_{\text{ch}} \gg T_{\text{asc}}$ and the chamber evolution timescale is much longer than the ascent timescale, rendering the transient terms negligible. In this limit, the time-dependent solution should equal the steady-state solution evaluated at the identical chamber pressure. Conversely, as $T_{\text{ch}} \sim T_{\text{asc}}$, the transient terms become non-negligible, requiring the full time-dependent solver. When gas escape is present, vertical and lateral gas escape timescales, taken at the depth of percolation threshold $z_{\phi g c}$,

$$T_{\text{vert}} = \left.\frac{z}{(v_g - v)}\right|_{z=z_{\phi g c}}, \quad T_{\text{lat}} = \left.\frac{R}{u_g}\right|_{z=z_{\phi g c}}, \tag{25}$$

may complicate the relationship between T_{ch} and T_{asc} depending on the value of k_c.

3.4 Initial conditions

After specifying boundary conditions at $t = 0$, we initialize the conduit system with the steady-state solution, where transient terms and dp_{ch}/dt are set to zero [e.g. *de' Michieli Vitturi et al.*, 2010; *Anderson and Segall*, 2011]. Code for the steady-state conduit flow was developed in *Wong et al.* [2017]. We consider cases where there may be non-unique initial conditions. Most steady-state solutions will not exactly satisfy the time-dependent system equations, requiring MATLAB to call the `daeic3` function to perturb this trial solution to find consistent initial conditions. Natural eruptions clearly do not start from steady-state and future work is required to develop more realistic eruption onsets.

3.5 Summary of model parameters

The forward model requires specification of magma chamber properties (aspect ratio, volume, recharge rate), conduit geometry (length, radius), material properties (conduit wall friction, magma permeability scale and percolation threshold), and conduit base

Table 2. Model parameter values for the nominal model, the model producing non-unique steady-state (ss) solutions, the models for analyzing the impact of gas escape, and the range applied in the Distance-based Generalized Sensitivity Analysis (DGSA).

Symbol	Description	Nominal	Non-unique ss	Gas escape analysis	DGSA range
Chamber properties					
α	Aspect ratio (width/height)	0.66	0.66	0.66	$0.5 - 1$
V_0	Volume (km^3)	100	$10^0 - 10^4$	10	$10 - 200$
Ω	Recharge rate (m^3 day^{-1} Pa^{-1})	0	0	0	0
Conduit geometry					
L	Length (km)	4	4	4	$2 - 8$
R	Radius (m)	50	100	50	$30 - 100$
Material properties					
f_0	Nominal coefficient of friction	0.1	0.1	0.1	$0.01 - 0.6$
a	Rate-dependence of friction	10^{-2}	10^{-2}	10^{-2}	$10^{-3} - 10^{-1}$
k_c	Magma permeability scale (m^2)	10^{-13}	10^{-14}	$0, 10^{-16} - 10^{-9}$	$10^{-20} - 10^{-10}$
ϕ_{gc}	Percolation threshold	0.3	0.3	0.3	$0.2 - 0.4$
Conduit base boundary conditions					
Δp_0	Excess pressure at $t = 0$ (MPa)	19	$2 - 10$	19	$10 - 30$
χ_h^{ch}	Total water content (wt%)	5	5	5	$3 - 7$
χ_c^{ch}	Total carbon dioxide content (ppm)	2000	2000	2000	$100 - 8000$

boundary conditions (initial pressure, volatile contents) (Table 2). The chamber depth is uniquely determined from the chamber volume, aspect ratio and conduit length.

To allow for a consistent description of the initial conduit base pressure for different conduit lengths, the total pressure at the conduit base p_{ch} is defined in terms of an excess pressure Δp_0 at $t = 0$,

$$p_{ch}(t = 0) = p_{atm} + \rho_l g L + \Delta p_0(t = 0), \qquad (26)$$

where p_{atm} is the pressure at the top of the conduit and ρ_l is the melt phase density. This excess pressure is not strictly the pressure over magmastatic because the density depth profile is not known *a priori*.

4 Results: Comparing time-dependent and steady-state solutions

In this section, we first illustrate typical model behavior through time-dependent solutions with nominal parameters. Next, we compare time-dependent solutions with steady-state solutions considering the scaling analysis in Section 3.3. We subsequently delve deeper into the effects of gas escape.

4.1 Time-dependent solution with nominal parameters

The nominal model produces a total extruded volume close to the 2004-2008 eruption of Mount St. Helens but is not necessarily a best-fit solution (Figure 3; parameters given in first column of Table 2). Magma outflow from the chamber to the conduit induces decay of chamber pressure (Figure 3a(i)). Since we prescribe zero chamber recharge in this model, the chamber pressure decays monotonically. As the driving pressure gradient declines, the magma velocity decreases. At the surface, magma exiting the conduit ("exit velocity") initially flows at 2.1×10^{-3} m/s but drops two orders of magnitude to 1.2×10^{-5} m/s after 4 years (Figure 3a(iii)). Slower magma flow allows more time for gas to escape, causing the exit porosity to decrease from 37% to 16% (Figure 3a(ii)).
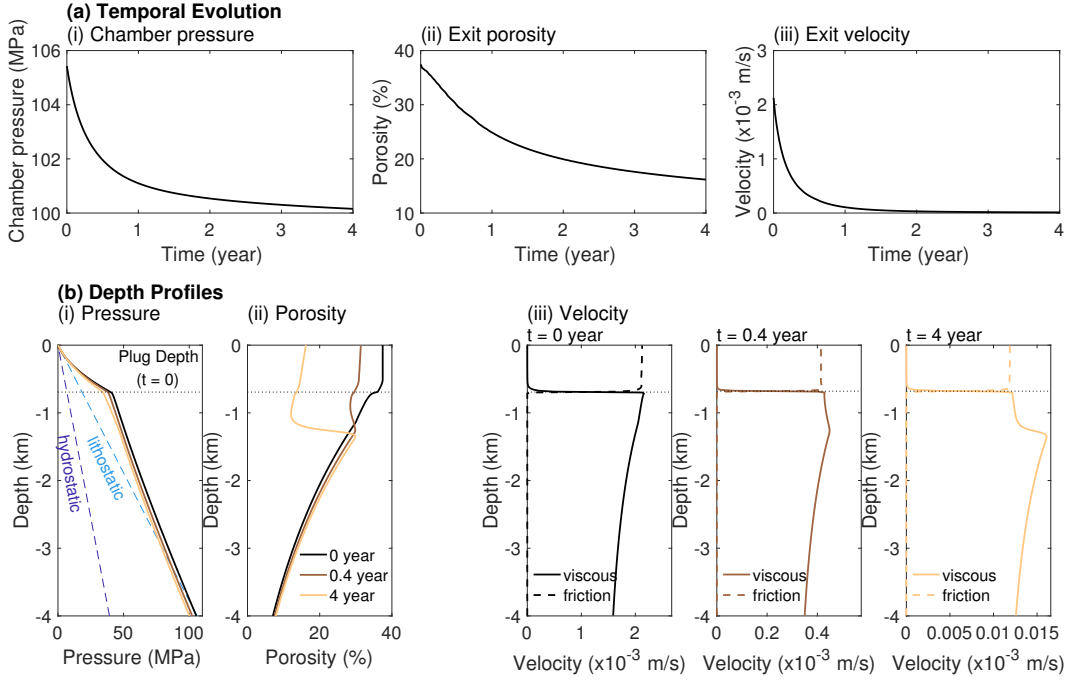
Figure 3. The nominal parameter model. (a) Temporal evolution of (i) chamber pressure, (ii) exit porosity and (iii) exit velocity. (b) Depth profiles of (i) pressure, with assumed hydrostatic and lithostatic pressure profiles are given in blue dashed lines, (ii) porosity and (iii) velocity at three times (0, 0.4 and 4 years; note different horizontal scales). The plug depth at $t = 0$ is indicated in the black dotted lines.

The feedback between slower velocity and decreasing porosity is clarified by examining depth profiles (Figure 3b). Throughout the eruption, the difference between conduit pressure and far-field hydrostatic pressure suggests considerable potential for lateral gas escape. This potential can only be realized at shallow depths once the magma has reached the percolation threshold, which occurs at 1.13 km depth at $t = 0$. Early in the eruption, magma velocity is high enough to replenish volatiles to this region, limiting the effect of gas escape. Gas exsolution and decompression promote higher porosity as magma approaches the surface.

As the eruption progresses, the magma velocity decreases which lowers the volatile supply. Gas escape can now counteract the effect of gas exsolution and decompression on porosity, reducing the porosity above the percolation threshold. In the fourth year of the eruption, depth profiles of porosity show a drop of nearly 20% above the percolation threshold at 1.24 km depth. This decline in porosity increases the weight of the magma column, leading to a decrease in velocity above the percolation threshold.

4.2 Effect of decaying chamber pressure on mass flow rate

When decreasing chamber pressure is accompanied by a decrease in mass flow rate at the conduit inlet (i.e. positive dp_{ch}/dq), solutions are stable. In contrast, when dp_{ch}/dq is negative, solutions can be unstable causing abrupt changes [*Slezin*, 2003; *Kozono and Koyaguchi*, 2012]. We examine this $p_{ch} - q$ relationship to compare steady-state and time-dependent solutions. Steady-state solutions were first obtained for a range of chamber pressures using the code in *Wong et al.* [2017]. Subsequently, time-dependent solutions were evaluated using a few steady-state initial conditions with different chamber volumes, which give different timescales for chamber pressure evolution, T_{ch}.

360 For the nominal parameter set (Figure 4a), steady-state solutions exhibit only pos-
361 itive dp_{ch}/dq, therefore steady-state solutions are unique. Time-dependent solutions with
362 large $T_{rat} = T_{ch}/T_{asc}$ (e.g. $V_0 = 10^4$ km^3) track the steady-state solutions. However, for
363 smaller T_{rat} (smaller chamber volumes), time-dependent solutions show greater deviation
364 from the steady-state solutions, consistent with the scaling analysis in Section 3.3. The
365 deviation is more pronounced at low mass flow rates, when the magma ascent timescale
366 increases.
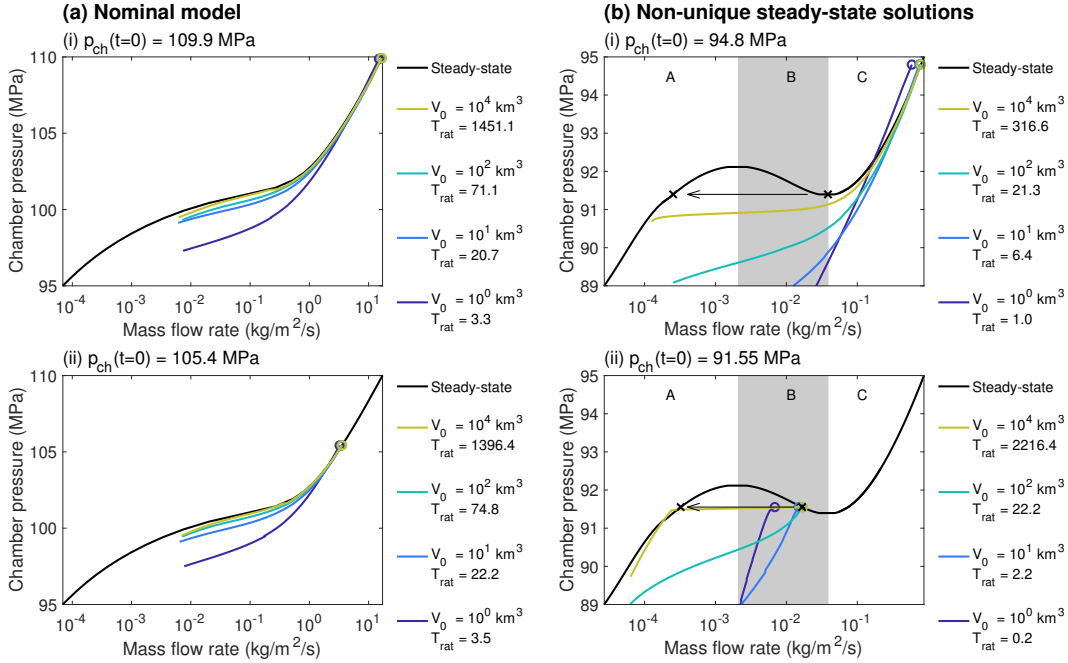
367 **Figure 4.** Relationship between chamber pressure and mass flow rate at the conduit inlet for two models:
368 (a) The nominal parameter model with initial chamber pressure (i) 109.9 MPa and (ii) 105.4 MPa. (b) A
369 model with non-unique steady-state solutions with initial chamber pressure (i) 95.05 MPa in stable solution
370 region C and (ii) 91.55 MPa in unstable solution region B. In each plot, black lines are steady-state solutions,
371 while blue to yellow lines are time-dependent solutions with different chamber volumes and therefore differ-
372 ent T_{rat}. Open circles denote the initial condition for time-dependent solutions. In (b), crosses with arrows
373 indicate the expected jump in mass flow rate across non-unique steady-state solutions.

374 Some parameter sets produce non-unique steady-state solutions within a range of
375 chamber pressures [*Wong et al.*, 2017] (Figure 4b). Here, $k_c = 10^{-14}$ m^2 and $R = 100$
376 m, while all other parameters are maintained at the nominal values (second column in Ta-
377 ble 2). Between 91.4 MPa and 92.2 MPa, two stable solutions and one unstable solution
378 exist for the steady-state system. When chamber pressure decreases to the boundary be-
379 tween Regions B and C, mass flow rate in the steady-state solution is expected to jump
380 across Region B and reach the stable steady-state solution with the corresponding chamber
381 pressure in Region A [e.g. *Kozono and Koyaguchi*, 2012]. For large T_{rat} ($V_0 = 10^4$ km^3),
382 where time-dependent solutions approach the steady-state limit, this abrupt decrease in
383 mass flow rate at nearly constant chamber pressure is observed (Figure 4b(i)). However,
384 for smaller chamber volumes, this decrease in mass flow rate is moderated. Note that the
385 time-dependent initial conditions are slightly offset from the steady-state curve due to per-
386 turbation by the numerical solver to find consistent initial conditions. The offset is largest
387 for small T_{rat} since these models are furthest from the steady-state approximations.

388 For time-dependent solutions initialized with steady-state solutions in the unstable
389 region (Region B), a similar abrupt decrease in mass flow rate is observed (Figure 4b(ii)).
390 For the largest T_{rat}, a slight chamber pressure decrease causes the time-dependent solu-
391 tion to transition from the unstable solution to the corresponding stable solution at a lower
392 mass flow rate. Further pressure decrease results in behavior that approximates the steady-
393 state solutions. In contrast, smaller chamber volumes show moderated decrease in mass
394 flow rate. As in Figure 4b(i), time-dependent initial conditions are offset from the steady-
395 state solutions.

4.3 Difference in gas escape behavior in time-dependent and steady-state models

397 The magma permeability scale k_c determines $k_{\text{vert}}, k_{\text{lat}}$ (equations 14, 15) to influ-
398 ence which terms dominate the volatile mass balance. In this section, all model parame-
399 ters are kept at nominal values except k_c and V_0 (third column in Table 2), which was set
400 to 10 km^3 to highlight differences between time-dependent and steady-state solutions. We
401 first obtain time-dependent solutions, then extract the chamber pressure time series to use
402 as boundary conditions for the steady-state approximations. For this V_0, T_{rat} ranges from
403 27 ($k_c = 0 \, \text{m}^2$) to 22 ($k_c = 10^{-9} \, \text{m}^2$).

404 In both time-dependent and steady-state solutions for this parameter set, a decrease
405 in chamber pressure induces a monotonic decrease in mass flow rate (Figure 5). For $k_c \leq$
406 $10^{-12} \, \text{m}^2$, mass flow rate in the time-dependent solutions is higher than the steady-state
407 solutions at the same pressure, as in Section 4.2. However, for $k_c > 10^{-12} \, \text{m}^2$, mass flow
408 rate in the time-dependent solutions is considerably lower than the steady-state solutions
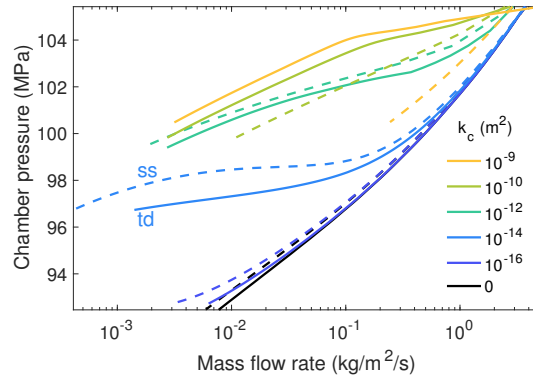409 at the same pressure.

Figure 5. Effect of magma permeability constant k_c on the chamber pressure-mass flow rate relation-
ship, comparing time-dependent solutions (td, solid lines) and steady-state approximations (ss, dashed
lines). Model parameters given in third column of Table 2. Timescale ratio $T_{\text{rat}} = 27 \, (k_c = 0 \, \text{m}^2)$ to
$22 \, (k_c = 10^{-9} \, \text{m}^2)$.

414 We examine the volatile mass balance equations (equation 11, 12) to determine the
415 effect of the transient term on conduit porosity and therefore the relationship between
416 chamber pressure and mass flow rate. For low k_c $(0, 10^{-16} \, \text{m}^2)$, lateral and vertical gas es-
417 cape can be neglected as their timescales are much longer than the magma ascent timescale
418 (Figure 6). In the steady-state solutions, the flux term is therefore zero: exsolution de-
419 creases the dissolved volatile content and decompression decreases the gas density, thus
420 porosity must increase as magma ascends (Figure 7a(i)). In the time-dependent solutions,
421 decreasing volatile content and gas density increases porosity in *time*. The transient term
422 thus enhances porosity increase (Figure 7b(i)) and lowers the magma column weight rela-
423 tive to the steady-state solution, therefore velocity throughout the conduit is higher. Den-

sity at the conduit base, where mass flow rate is calculated, is approximately the same for both solutions. Combining the increased velocity with the approximately equal density produces a higher mass flow rate for time-dependent solutions.
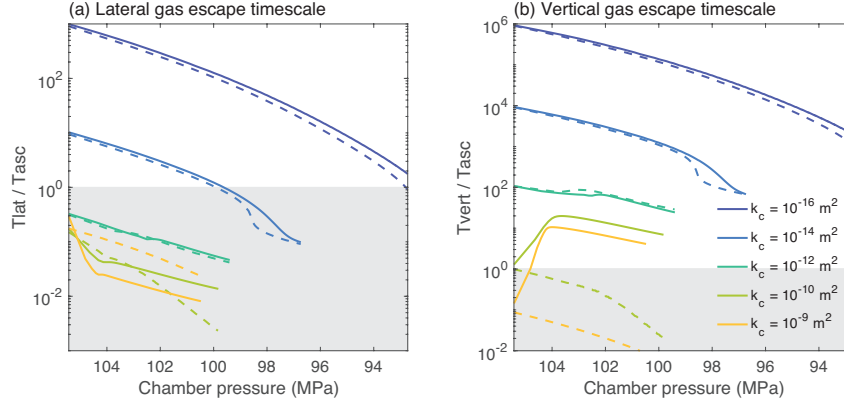

Figure 6. (a) Lateral and (b) vertical gas escape timescales compared to the ascent timescales for models with different magma permeability scale k_c. Solid lines are time-dependent solutions, while dashed lines are steady-state approximations. When the curves enter the gray shaded region, gas escape can significantly influence mass balance in the conduit.

For intermediate k_c ($10^{-14}, 10^{-12}$ m²), porosity initially increases with decreasing pressure in the steady-state solutions as a result of gas exsolution and decompression as in the low k_c case (Figure 7a(ii)). However, as the chamber pressure and therefore magma velocity become smaller, the lateral gas escape timescale eventually becomes shorter than the magma ascent timescale (Figure 6), and porosity above the percolation threshold decreases. Vertical gas escape is still negligible as the vertical gas escape timescale is still much longer than the magma ascent timescale. In the time-dependent solutions, porosity increases at early times to a greater extent due to the transient term enhancing porosity increase (Figure 7b(ii)). The enhanced porosity continues even after lateral gas escape becomes appreciable. In addition, the transient term in the volatile mass balance in the plug permits plug porosity variations in depth (equation A.1). Since porosity is consistently higher than the steady-state solutions, magma velocity and thus mass flow rate are higher.

For high k_c ($10^{-10}, 10^{-9}$ m²), lateral and vertical gas escape dominate volatile mass balance above the percolation threshold (Figure 6). In the steady-state solutions above the percolation threshold, gas ascends through the column primarily by vertical gas escape and is subsequently lost through lateral gas escape (Figure 7a(iii)). Each steady-state solution is independent and adjusts to ensure that magma flux into the base of the permeable zone sustains gas escape. The magma column remains more gas-rich and maintains higher mass flow rate. In the time-dependent solutions, high magma permeability allows a large proportion of volatiles to be lost to the surroundings at early time. Subsequent input from magma flux at the percolation threshold is insufficient to compensate for gas escape, thus porosity drops considerably (Figure 7b(iii)). The magma column weight increases and the mass flow rate decreases substantially. Since magma permeability is proportional to the third power of porosity, magma permeability subsequently drops to very low values and further volatile loss is moderated.
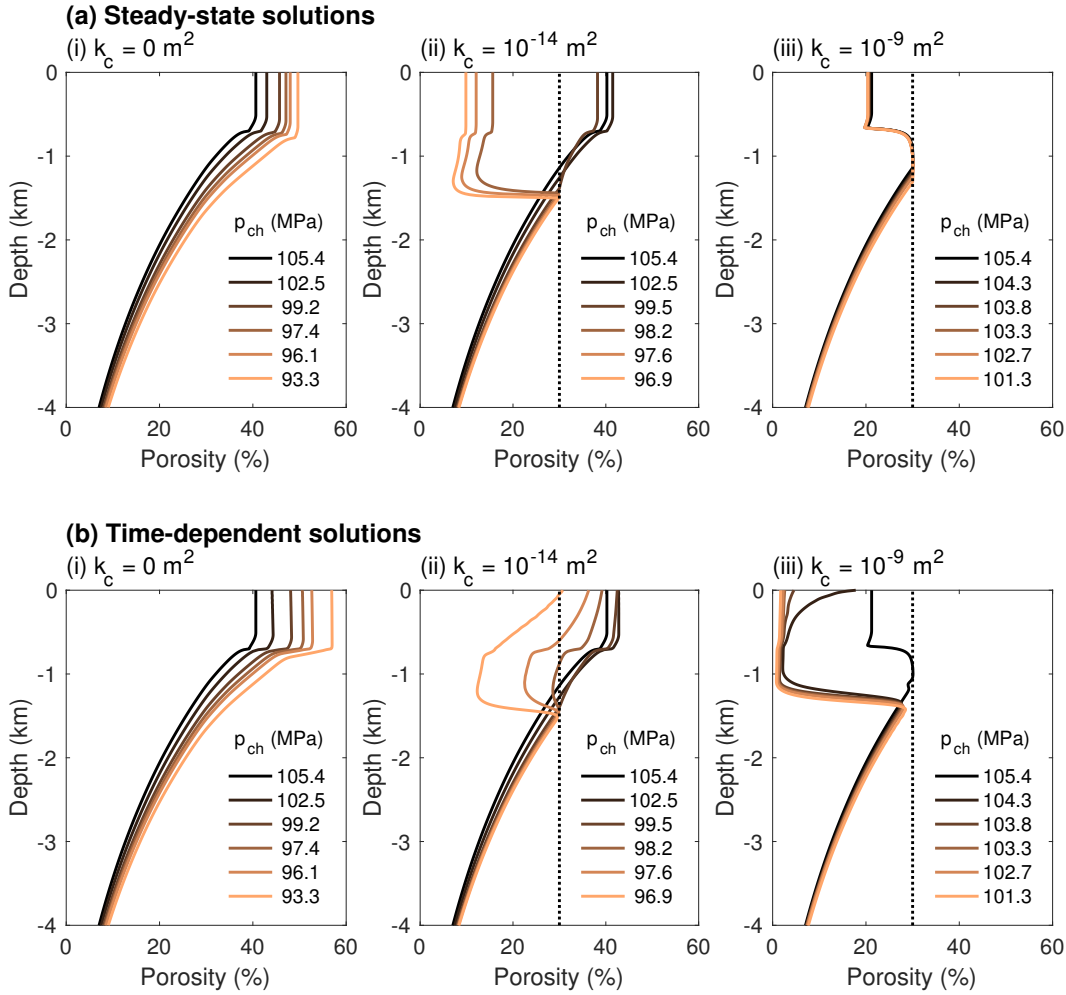
(a) Steady-state solutions

(b) Time-dependent solutions

Figure 7. Depth profiles of porosity at different chamber pressure p_{ch} of the (a) steady-state solutions and (b) time-dependent solutions for three k_c values. The vertical dotted line is the percolation threshold (set to 30%). There is no percolation threshold for $k_c = 0$.

5 Application of time-dependent model to 2004-2008 Mount St. Helens eruption

5.1 Calculating observables from model outputs

At Mount St. Helens, renewed swarms of earthquakes began on September 23, 2004, followed by a series of explosions beginning October 1, 2004 [*Moran et al.*, 2008; *Scott et al.*, 2008]. These vent-clearing explosions coincided with rapid movement of JRO1, the only nearby continuous GPS station located at the Johnston Ridge Observatory around 10 km north of the summit, towards the volcano at 0.5 mm/day [*Lisowski et al.*, 2008]. Extrusion in the crater resulted in a large welt in the crater glacier that gave way to a lava spine, first seen on October 11, 2004, on the south side of the 1980s lava domes [*Vallance et al.*, 2008; *Scott et al.*, 2008; *Dzurisin et al.*, 2015]. Thereafter, a series of lava spines, some of which resembled "whalebacks", were extruded on the crater floor accompanied by tilt cycles [*Vallance et al.*, 2008; *Anderson et al.*, 2010] and repetitive low-frequency and hybrid "drumbeat" earthquakes that were postulated to have been produced by stick-slip motion of a solid plug ascending through the conduit [*Moran et al.*, 2008; *Iverson*, 2008]. After 3.3 years, eruptive activity waned and finally ended in January 2008 [*Dzurisin et al.*, 2015].

During the eruption, a wide variety of data was collected. Three time-varying datasets were chosen to compare with model predictions (Figure 8): (a) extruded volume which indicates the evolution of exit velocity, (b) gas emissions which inform us about volatile content and permeability, and (c) ground deformation which reflects pressure change and geometry of the magma reservoir. These datasets target different parts of the chamber-conduit system and could potentially reveal less obvious interactions among magmatic processes.
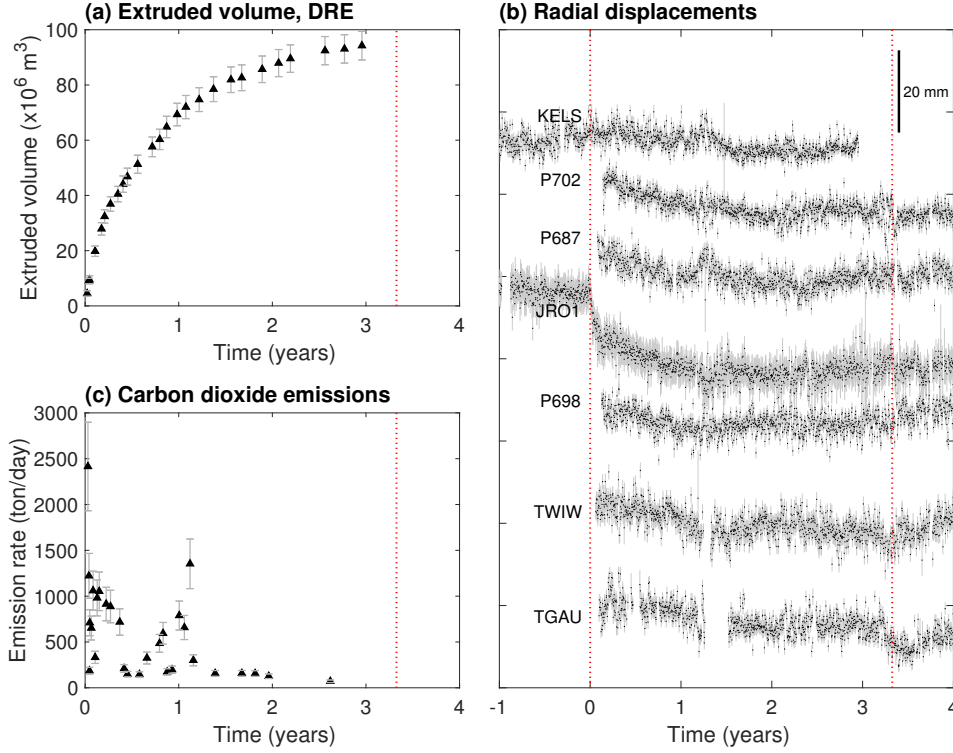
Figure 8. Time-series data sets from the 2004-2008 eruption of Mount St. Helens. (a) Dense rock equivalent (DRE) of cumulative extruded lava volume. (b) Radial displacements at 7 GPS stations, sorted by furthest (KELS) to nearest (TGAU) to the volcano edifice. (c) Carbon dioxide emissions. Vertical red dotted lines indicate start and end times of the eruption. Data sources described in text.

Extruded volume is converted to its dense rock equivalent by removing the bubble fraction and integrating exit velocity over time [*Anderson and Segall*, 2011],

$$V_{\text{ex}}(t) = \pi R^2 \int_0^t v(z = 0, t)[1 - \phi_g(z = 0, t)] \, dt, \tag{27}$$

The predicted volume was then compared with data collected from differential Digital Elevation Models (DEMs) [*Schilling et al.*, 2008; *Dzurisin et al.*, 2015]. As in *Anderson and Segall* [2013], we add the initial welt growth of approximately 10 million m³ on October 11, 2004, to reflect subglacial extrusion, then remove an estimated dome porosity of 10% to obtain the dense rock equivalent (DRE) volume [*Gerlach et al.*, 2008]. Volume uncertainties arise from the welt volume approximation ($\sim$ 1 million m³) and from the DEM volume estimates ($\sim$ 4%) [*Schilling et al.*, 2008]. The total extruded volume reached a maximum of 94.2 million m³ (Figure 8a). Post-eruption volume decline is attributed to dome compaction.

Of all the continuous GPS stations near Mount St. Helens, only JRO1 was in operation before the eruption onset and captured rapid deflationary motion of about 10 mm in the initial few weeks of the eruption, followed by slower deflation of an additional 10 mm [*Lisowski et al.*, 2008; *Anderson and Segall*, 2013] (Figure 8b). Another continuous GPS station, KELS, was far away from the vent ($\sim$ 50 km) and did not exhibit significant deformation. Other nearby stations were deployed one month after the eruption began and displayed only the later slow deflation. In this study, we focus on the JRO1 time series to explore possible reasons for this enigmatic temporal evolution of deformation. Radial displacements are calculated from the modeled pressure change in a spheroidal chamber using the expressions of *Yang et al.* [1988]. We do not consider the effect of conduit tractions on surface displacements, because JRO1 is far from the vent relative to the plug length.

Emissions of carbon dioxide generally decay with time, but with much greater scatter relative to the other data sets (Figure 8c). These data, along with measurements of sulfur dioxide and hydrogen sulfide, were collected via aircraft sampling of the vapor plume [*Gerlach et al.*, 2008]. Gases escaping both vertically through the conduit and laterally through the wall rocks may be observed at the surface. Laboratory measurements reveal that vertical permeability of the dome was several orders of magnitude larger than the lateral permeability, suggesting that gases primarily escaped vertically through the highly permeable fracture networks in the marginal shear zone [*Gaunt et al.*, 2014]. Gases escaping laterally would experience a time delay before being observed at the surface due to percolation through the surrounding crust. Based on observations of *Gerlach et al.* [2008] and *Dzurisin et al.* [2015], emissions of CO_2 and SO_2 declined below the detection limit before the eruption ceased, indicating either that lateral gas escape is minor, that the amount of these gases reaching the surface is small, or that the lag time is short. It is worth noting, however, that Loowit Springs on the north side of the volcano exhibited an increase in ^{13}C in water samples and CO_2 in bubble gas, suggesting that magmatic gases may have been transported laterally out of the conduit [*Bergfeld et al.*, 2017]. Further examination of this is necessary to determine the effect of subsurface gas transport on gas emissions and spring chemistry changes. For this study, we approximate that all CO_2 observed in the plume escaped vertically and calculate the carbon dioxide emissions as

$$Q_c^{ex}(t) = \pi R^2 \frac{\Gamma}{1 + \Gamma} \rho_g \phi_g (v_g - v) \Big|_{z=0} \tag{28}$$

where all variables are evaluated at the surface using the plug gas loss approximation (equation A.1). Note that there is also flux of gas transported within pores in the magma, however, this contribution is small since v is much smaller than $(v_g - v)$ at the surface.

5.2 Sensitivity of time-series observables to model parameters

With higher initial chamber pressures, the predicted time-series data exhibit larger amplitudes and faster temporal evolution of extruded volumes, radial displacements and carbon dioxide emissions (Figure 9). These models are identical to the nominal model but with initial excess pressures of $15 - 23$ MPa. High initial chamber pressure produces rapid outflux from the chamber, causing faster decay of chamber pressure and depressing subsequent velocities. The nominal model ($p_{ch} = 105$ MPa) matches the observed amplitudes but not the temporal evolution of all three datasets. Although the model is not able to capture the observed variations in carbon dioxide emissions, the order of magnitude and overall trend agrees with the observations.

To examine the sensitivity to model parameters more generally, we perform a Distance-based Generalized Sensitivity Analysis (DGSA) on 1100 randomly-sampled model realizations evaluated to $t = 4$ years [*Fenwick et al.*, 2014]. Unlike many other sensitivity measures (e.g. the Sobol indices method), DGSA analyzes the full time series and requires a smaller number of realizations. We refer the reader to details of the DGSA procedure in *Fenwick et al.* [2014]. Here we employ the DGSA Matlab toolbox developed in *Park et al.*
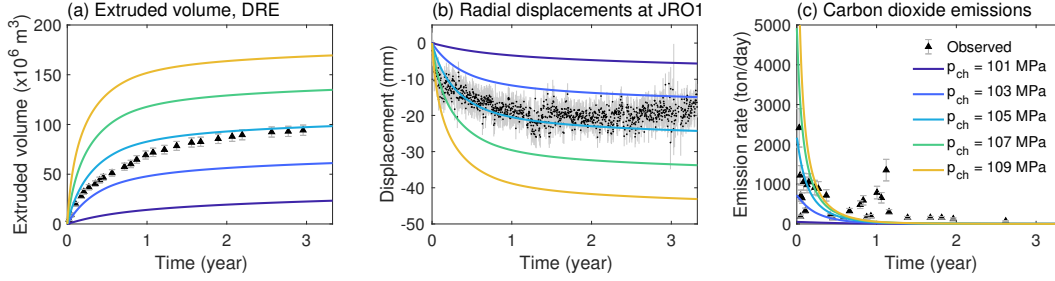
Figure 9. Predicted time-series data from model realizations with increasing initial chamber pressure $p_{ch}(t = 0)$. All other model parameters are at nominal values. (a) DRE extruded volume, (b) radial displacements at JRO1, and (c) carbon dioxide emissions.

[2016] to calculate and visualize model sensitivity. We include figures illustrating intermediate DGSA steps in Section S3 of the Supplementary Information.

Model parameter ranges for DGSA are given in Table 2. In all analyses, chamber recharge rate Ω was set to zero as this will otherwise dominate model predictions. For the 1100 model realizations, T_{ch}/T_{asc} ranges from 1 - 1000 (Figure S3). We apply DGSA to measure sensitivity of extruded volume, radial displacement and carbon dioxide emissions, first on the full time series responses and second on the responses normalized by their final value (Figure 10). In analyzing the full time series, DGSA classifies model predictions primarily by their final values (Figure S4a). In analyzing the normalized time series, DGSA classifies model predictions primarily by their temporal evolution (Figure S4b).

In a simple model of a deflating elastic magma chamber with constant magma properties [e.g. *Segall*, 2013], total extruded volume scales with $(\beta_{mag} + \beta_{ch})(p_{ch} - p_{mag})V_0$, where p_{mag} is the magmastatic pressure. As predicted by this simple model, extruded volume magnitude is sensitive to chamber volatile contents χ_h^{ch}, χ_c^{ch}, which affect β_{mag} and p_{mag}, and chamber volume V_0 (Figure 10a(i)). Extruded volume is also sensitive to excess pressure Δp_0 and conduit length L which both determine p_{ch} (equation 26). Not all models reach their asymptotic limit at the simulation end time ($t = 4$ years), therefore extruded volume is also sensitive to parameters that affect the extrusion rate (conduit radius R, friction parameters f_0, a). Total extruded volume is not sensitive to chamber aspect ratio α, magma permeability scale k_c and the percolation threshold ϕ_{gc}.

The temporal evolution of extruded volume is most sensitive to R, a, k_c and Δp_0 (Figure 10a(ii)). Strong sensitivity to R is expected since conduit area and velocity are each proportional to R^2 (equation 8), thus magma volume flux (rate of change of extruded volume) is proportional to R^4. The rate-dependence of friction a determines the friction coefficient as velocity decreases with time, while k_c combined with porosity which is a time-dependent quantity, determines magma permeability (equation 14).

Radial displacements measured at the location of station JRO1 are most sensitive to V_0 and Δp_0 which scale the deformation source strength (Figure 10b(i)). Water content χ_h^{ch} affects the porosity and therefore magmastatic pressure, thus determining the extent of pressure decay. Other parameters V_0, L, α implicitly define the chamber depth. Parameters that affect chamber outflux and therefore the rate of chamber pressure decay (conduit radius R, friction parameters f_0, a) are influential because not all models have reached their asymptotic limit of magmastatic pressure. The normalized time series of deformation is affected by a similar order of parameters as the normalized extruded volume time series, emphasizing the role of k_c, a in affecting temporal evolution but not total displacements (Figure 10b(ii)).
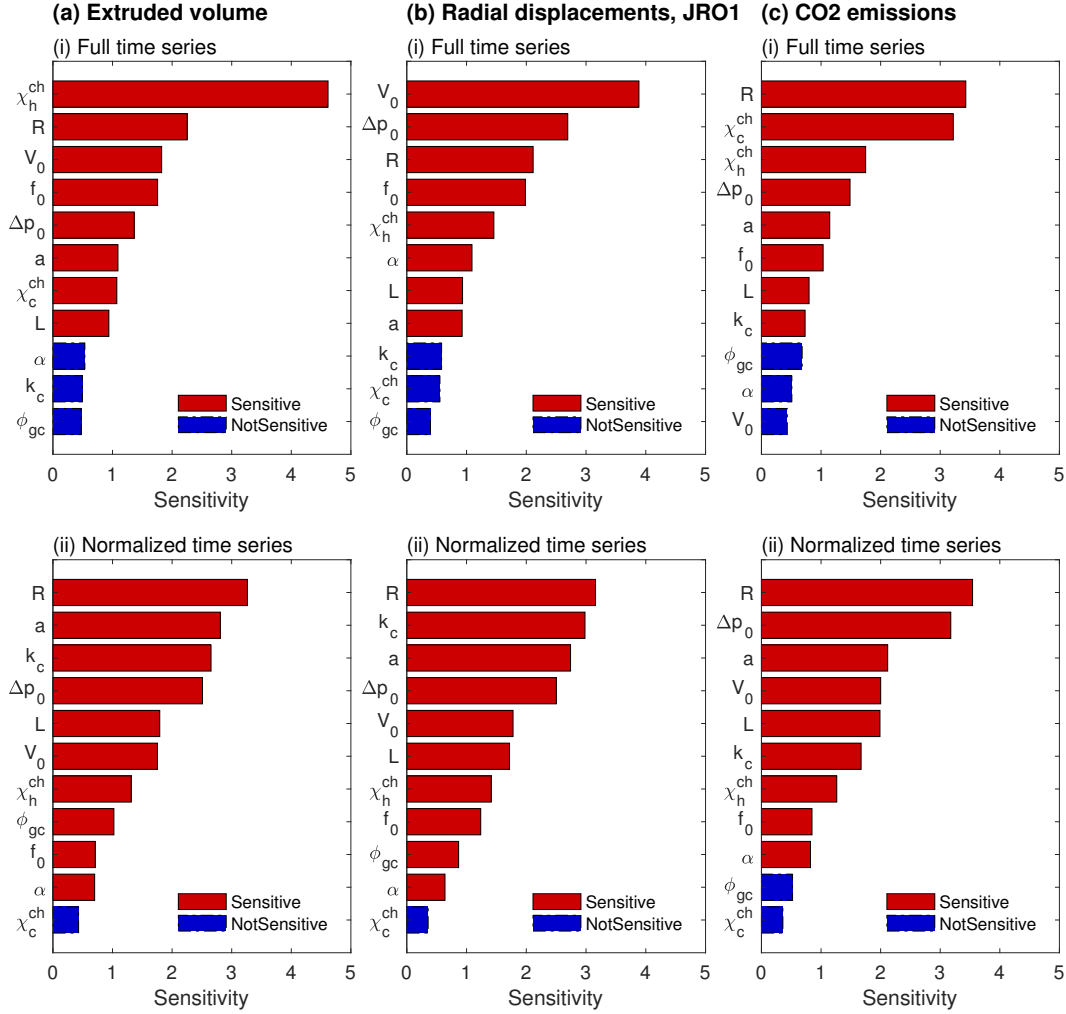
Figure 10. Pareto plots quantifying sensitivity of time series responses of (a) extruded volume, (b) radial displacements at JRO1, and (c) carbon dioxide emissions. Top row shows sensitivity of the full time series where model realizations are classified by their magnitude at $t = 4$ years, while bottom row shows sensitivity of the normalized time series where model realizations are classified by their temporal evolution.

Initial carbon dioxide emissions are most sensitive to R, χ_c^{ch} (Figure 10c(i)), since emissions are proportional to R^2 (equation 28) and the χ_c^{ch} supplies the carbon dioxide. Other parameters ($R, \chi_h^{ch}, \Delta p_0, a, f_0, L$) influence the rate of magma ascent and therefore the carbon dioxide flux from depth. Carbon dioxide emissions are not very sensitive to k_c, ϕ_{gc} since gas percolation close to the surface is controlled by plug gas loss (equation A.1). The normalized time series has a similar sensitivity ranking to the other two normalized datasets. However, k_c has a lesser role since it does not control gas percolation in the plug. Chamber carbon dioxide content does not influence the temporal evolution of carbon dioxide emissions because it is modeled as constant through time and other parameters determine the eruption decay behavior (Figure 10c(ii)).

6 Discussion

6.1 Evaluating the difference between time-dependent and steady-state solutions

Scaling analysis of the solids and liquids continuity equations indicates that for $T_{rat} = T_{ch}/T_{asc} \gg 1$, time-dependent solutions should approach the steady-state limit (equation 22). The numerical model here reaches the steady-state limit at $T_{rat} \sim 10^2$. This large critical value suggests that gas escape, particularly from the plug gas loss approximation, may complicate the approach to steady-state. We employ the plug gas loss approximation because it is consistent with the observed low dome porosity and only requires a simple modification of the continuity equations. However, this approximation does not account for how gas overpressure establishes enhanced permeability in the plug. At a given chamber pressure, transient terms in the volatile mass balance allow vertical gradients in porosity to develop in the plug, delaying the approach to steady-state. Consideration of the physics of fracturing and compaction in the plug would provide an estimate of the timescale for the plug to reach steady-state, therefore improving the estimate of the critical T_{rat}.

Time-dependent solutions below this critical T_{rat} do not match steady-state approximations. Model parameter sets with non-unique steady-state solutions predict a jump in mass flow rate as chamber pressure decreases (Section 4.2). In contrast, time-dependent solutions do not show this jump in mass flow rate. The assumptions of equilibrium crystallization and rate-strengthening friction stabilize the temporal evolution of flow. As the eruption progresses, decreasing conduit pressure results in more crystallization, resisting flow. In addition, decreasing plug velocity reduces the frictional resistance to flow. Both effects prevent sudden drops or surges in mass flow rate.

For different k_c, transient effects influence volatile mass balance in different ways (Section 4.3). At a given chamber pressure, low k_c models produce higher mass flow rates relative to the steady-state approximations because the transient term compounds the effect of gas exsolution and decompression, causing porosity to increase with time (Figure 5). In contrast, high k_c models produce lower mass flow rates relative to the steady-state approximations because mass flux cannot replenish gas escaped through lateral and vertical gas transport. This complex, non-monotonic relationship suggests that model predictions may be significantly biased if steady-state solutions are used as approximations for analyzing time-series data.

Given the current model setup, estimates of chamber volume at Mount St. Helens suggest that time-dependent solutions are needed to analyze time-series data of the dome-forming eruption. Deformation [e.g. *Lisowski et al.*, 2008] and seismic velocity models [e.g. *Kiser et al.*, 2016] suggest a prolate ellipsoidal chamber with axes of 5-10 km, corresponding to volumes of $100 - 1000$ km^3. Inversions of extruded volume and deformation also prefer chamber volumes of $100 - 200$ km^3 [*Anderson and Segall*, 2013]. With these chamber volumes, steady-state solutions are poor approximations to the time-dependent solution. Only for much larger chamber volumes ($\sim 10^4$ km^3), steady-state solutions are sufficient approximations to the temporal evolution of an eruption in this model.

6.2 Implications of the sensitivity analysis for the Mount St. Helens magmatic system

DGSA reveals the most influential parameters determining the magnitude of extruded volume and displacements to be chamber water content, chamber volume, conduit radius and excess pressure. For carbon dioxide emissions, the chamber carbon dioxide content is also influential. Main parameters determining the temporal evolution behavior are the conduit radius, rate-dependence of friction and magma permeability scale. For almost all the predicted datasets, percolation threshold and chamber aspect ratio have limited influence.

6.2.1 Deformation at JRO1

Previous work by *Anderson and Segall* [2013] did not physically model the rapid radial motion at JRO1 in the initial weeks of the eruption. Instead, model outputs were combined with an empirical fit to an exponential decay for the "vent-clearing" phase to simulate the deformation time series. Failure to model the physics of this first phase of the eruption could bias model estimates, for example underestimating the decrease in chamber pressure.

We examine the impact of the three most sensitive parameters affecting the temporal evolution of displacements at JRO1: R, a, k_c (Figure 10b(ii)). We explore variations in these parameters together with initial excess pressure Δp_0 to produce models with similar displacements u_{end} at $t = 3.3$ years, the eruption duration. First, we examine variations in R and a with no explicitly-modeled gas escape, akin to *Anderson and Segall* [2011]. Increasing R while keeping chamber pressure constant should result in higher magma outflux from the chamber and therefore greater pressure decay, thus we need to reduce Δp_0 to obtain similar u_{end} (Figure 11a). This combination produces models of similar magma outflux. Pressure decay and therefore deflation rates are similar for all three R models, but are far too slow to fit the observed displacement time series. For the rate-dependence of friction a, reasonable parameter variations without gas escape are also unable to explain the rapid deflation in the first few weeks of the eruption. At $t = 0$, higher a corresponds to greater frictional resistance, requiring higher Δp_0 to obtain similar u_{end} (Figure 11b). However, higher a also means that when the velocity declines during the eruption, the frictional resistance declines more substantially. This moderates the decrease in velocity and chamber pressure.

When gas escape is included in the model, increasing k_c while keeping the same initial chamber pressure produces a smaller pressure decay (Figure 5). Therefore, to obtain similar displacements u_{end} at $t = 3.3$ years, higher k_c requires higher Δp_0. The higher Δp_0 facilitates a higher magma outflux and faster initial deflation rate (Figure 11c). However, high k_c also allows rapid loss of volatiles to decrease porosity and increase magma density. Transition to this low porosity conduit drives down the velocity, and also depresses the permeability, suppressing further gas escape. These effects prevent continued rapid pressure drop and deflation. Gas escape is therefore required in the present model to explain the rapid then muted deflation in the observed deformation time series.
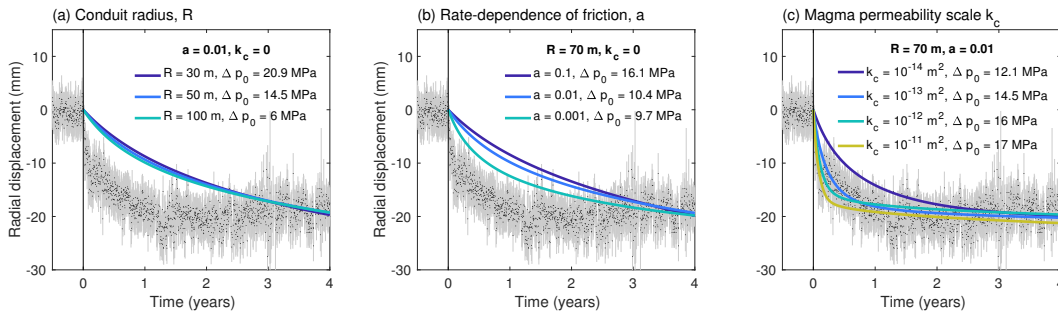

Figure 11. Comparing predicted radial displacements at JRO1 to observed displacements. (a) Impact of variations in conduit radius R and (b) rate-dependence of friction a when gas escape is omitted (i.e. $k_c = 0$). (c) Impact of variations in k_c. In all plots, the initial excess pressure Δp_0 is adjusted to produce displacement magnitudes close to observed values at $t = 3.3$ years.

7 Conclusion

The physics-based time-dependent 1D chamber-conduit model developed here simulates the evolution of magma flow through phase transitions and material changes during an effusive dome-forming eruption. The inclusion of pressure-dependent magma solidification, solid fraction-dependent viscosity and gas escape from the conduit allows magma to naturally transition from a viscous flow regime to frictional sliding, reflecting the behavior in dome-forming eruptions. Time-dependent solutions were compared with steady-state approximations to understand the impact of transient processes. Predictions of the model were qualitatively compared with diverse time-series data from the 2004-2008 eruption at Mount St. Helens.

Key findings relating to conduit flow and model development include:

1. Rigorous testing using the method of manufactured solutions verifies the numerical method and demonstrates at least second order convergence.
2. Magma flow transitions from viscous flow to frictional sliding abruptly at the plug depth throughout the eruption. As velocity decreases, porosity above the percolation threshold decreases as more time allows for gas escape.
3. Scaling analysis indicates that time-dependent solutions should approach the steady-state limit when the chamber evolution timescale is much longer than the magma ascent timescale. This numerical model reaches the steady-state limit at $T_{\mathrm{rat}} \sim 10^2$, suggesting that the model for gas escape, particularly in the plug, may influence this approximation.
4. For low magma permeability scale k_c, the transient term can increase porosity and consequently magma mass flow rate relative to steady-state solutions. For high k_c, early removal of gas through efficient lateral and vertical gas transport depresses porosity and mass flow rate relative to steady-state solutions.
5. Distance-based generalized sensitivity analysis (DGSA) shows that the total extruded volume is sensitive to chamber water content, conduit radius and chamber volume, while total ground displacements are sensitive to chamber volume, chamber excess pressure and conduit radius. Initial carbon dioxide emissions are sensitive to conduit radius and chamber volatile contents. The temporal evolution of the three datasets are sensitive to conduit radius, rate-dependence of friction and magma permeability scale. Model predictions are mostly insensitive to percolation threshold and chamber aspect ratio.
6. Gas escape from the conduit can lead to marked departures from exponentially decaying eruption flux. Higher magma permeability models exhibit initially rapid then more gradual decay in magma velocity and chamber pressure, and may explain the distinctive deformation time series recorded at JRO1 during the Mount St. Helens eruption.

A: Implementation of permeability changes at shallow depth

A.1 Hysteretic permeability

Experiments show that the percolation threshold is lower in compacting magmas than in vesiculating magmas [*Rust and Cashman*, 2004; *Colombier et al.*, 2017]. To simulate this hysteretic behavior, once magma becomes permeable at the percolation threshold, its permeability is calculated at shallower depths according to equation 14 while ignoring the percolation threshold condition.

In the time-dependent equations, we additionally ensure that depths that allow permeable gas flow remain permeable for the eruption duration. To implement this switch, we store the depth of the percolation threshold at each time using persistent variables, which are retained in memory but can only be accessed within the specified function.

At the next time step, the solver checks the position of the percolation threshold relative to the previous time step: if it is deeper, the percolation threshold is adjusted to the new depth; if it is shallower, the percolation threshold is maintained at the previous depth since this depth cell is already permeable. The code then stores the new time and accepted depth for comparison at the next time step.

A.2 Gas flow in plug

In the plug, magma viscosity is high, which limits bubble expansion even as gases exsolve from the magma and gas density decreases due to depressurization. At this point, either porosity continues to increase considerably, gas overpressure develops, or gas has to escape to maintain gas pressure in equilibrium with the surrounding viscous and nearly solid magma. In the first option, a large porosity increase contradicts hand samples with low dome porosity (5-10%) from the recent Mount St. Helens eruption [*Cashman et al.*, 2008; *Smith et al.*, 2011]. In the second option, the timescale of bubble expansion through the viscous plug relative to magma ascent gives an estimate of the possible gas overpressure, $T_{\text{bubble}} = \eta/(p_{\text{gas}} - p)$ [*Gonnermann and Manga*, 2013]. Magma ascent allows bubbles to expand on the timescale of $L/v \sim 10^3/10^{-3} \sim 10^6$ s. Viscosity in the plug can reach 10^{16} Pa s, which allows a gas overpressure of 10^4 MPa in the bubbles. Such a large gas overpressure could prompt fragmentation, which was not observed in the Mount St. Helens eruption.

Consequently, we assume the third option as in *Wong et al.* [2017]. Gas exsolution and expansion is compensated by gas escape through enhanced permeability, such as through the formation of cracks (we call this "plug gas loss"). For the continuity equation of water (equation 11), this assumes balance of almost all depth-dependent terms,

$$\frac{\partial}{\partial z}\left(\chi_h^d \rho_l \phi_l c_1 v\right) + \frac{1}{1+\Gamma}\phi_g v \frac{\partial \rho_g}{\partial z} = -\frac{\partial}{\partial z}\left[\frac{1}{1+\Gamma}\rho_g \phi_g (v_g - v)\right] - \frac{2\rho_g \phi_g u_g}{R(1+\Gamma)}. \tag{A.1}$$

A similar form holds for the carbon dioxide mass balance. The conservation of mass for water (and similarly carbon dioxide) therefore reduces to

$$\frac{\partial}{\partial t}\left(\chi_h^d \rho_l \phi_l c_1 + \frac{1}{1+\Gamma}\rho_g \phi_g\right) = -\rho_g \frac{\partial}{\partial z}\left(\frac{1}{1+\Gamma}\phi_g v\right). \tag{A.2}$$

In the steady-state approximation, the transient term is absent, resulting in constant porosity and velocity in depth as shown in *Wong et al.* [2017]. In the time-dependent solution, the transient term permits gradients of magma velocity and porosity in depth.

References

Amoruso, A., and L. Crescentini (2009), Shape and volume change of pressurized ellipsoidal cavities from deformation and seismic data, *Journal of Geophysical Research: Solid Earth*, *114*(2), 1–8, doi:10.1029/2008JB005946.

Anderson, K., and P. Segall (2011), Physics-based models of ground deformation and extrusion rate at effusively erupting volcanoes, *Journal of Geophysical Research: Solid Earth*, *116*(7), 1–20, doi:10.1029/2010JB007939.

Anderson, K., and P. Segall (2013), Bayesian inversion of data from effusive volcanic eruptions using physics-based models: Application to Mount St. Helens 2004-2008, *Journal of Geophysical Research: Solid Earth*, *118*(March), 2017–2037, doi:10.1002/jgrb.50169.

Anderson, K., M. Lisowski, and P. Segall (2010), Cyclic ground tilt associated with the 2004-2008 eruption of Mount St. Helens, *Journal of Geophysical Research: Solid Earth*, *115*(11), 1–29, doi:10.1029/2009JB007102.

Bergfeld, D., W. C. Evans, K. R. Spicer, A. G. Hunt, and P. J. Kelly (2017), Evidence for degassing of fresh magma during the 2004-2008 eruption of Mount St. Helens: Subtle signals from the hydrothermal system, *Journal of Volcanology and Geothermal Research*, doi:10.1016/j.jvolgeores.2017.06.020.

Blanpied, M. L., C. J. Marone, D. a. Lockner, J. D. Byerlee, and D. P. King (1998), Quantitative measure of the variation in fault rheology due to fluid-rock interactions, *Journal of Geophysical Research*, *103*(98), 9691, doi:10.1029/98JB00162.

Blower, J. (2001), Factors controlling permeability-porosity relationships in magma, *Bulletin of Volcanology*, *63*, 497–504, doi:10.1007/s004450100172.

Caricchi, L., L. Burlini, P. Ulmer, T. Gerya, M. Vassalli, and P. Papale (2007), Non-Newtonian rheology of crystal-bearing magmas and implications for magma ascent dynamics, *Earth and Planetary Science Letters*, *264*(3-4), 402–419, doi:10.1016/j.epsl.2007.09.032.

Cashman, K. V., C. Thornber, and J. S. Pallister (2008), From Dome to Dust: Shallow Crystallization and Fragmentation of Conduit Magma During the 2004-2006 Dome Extrusion of Mount St . Helens, Washington, *A Volcano Rekindled: The Renewed Eruption of Mount St. Helens 2004-2006, U.S. Geological Survey Professional Paper 1750*, pp. 387–413.

Chevalier, L., M. Collombet, and V. Pinel (2017), Temporal evolution of magma flow and degassing conditions during dome growth, insights from 2D numerical modeling, *Journal of Volcanology and Geothermal Research*, *333*, 116–133, doi:10.1016/j.jvolgeores.2017.01.016.

Collombet, M. (2009), Two-dimensional gas loss for silicic magma flows: Toward more realistic numerical models, *Geophysical Journal International*, *177*(1), 309–318, doi:10.1111/j.1365-246X.2008.04086.x.

Colombier, M., F. B. Wadsworth, L. Gurioli, B. Scheu, U. Kueppers, A. Di Muro, and D. B. Dingwell (2017), The evolution of pore connectivity in volcanic rocks, *Earth and Planetary Science Letters*, *462*, 99–109, doi:10.1016/j.epsl.2017.01.011.

Costa, A. (2005), Viscosity of high crystal content melts: Dependence on solid fraction, *Geophysical Research Letters*, *32*(22), 1–5, doi:10.1029/2005GL024303.

de' Michieli Vitturi, M., A. B. Clarke, A. Neri, and B. Voight (2010), Transient effects of magma ascent dynamics along a geometrically variable dome-feeding conduit, *Earth and Planetary Science Letters*, *295*(3-4), 541–553, doi:10.1016/j.epsl.2010.04.029.

De' Michieli Vitturi, M., A. B. Clarke, A. Neri, and B. Voight (2013), Extrusion cycles during dome-building eruptions, *Earth and Planetary Science Letters*, *371-372*, 37–48, doi:10.1016/j.epsl.2013.03.037.

Denlinger, R. P., and R. P. Hoblitt (1999), Cyclic eruptive behavior of silicic volcanoes, *Geology*, *27*(5), 459–462, doi:10.1130/0091-7613(1999)027<0459.

Dzurisin, D., S. C. Moran, M. Lisowski, S. P. Schilling, K. R. Anderson, and C. Werner (2015), The 2004-2008 dome-building eruption at Mount St. Helens, Washington: epilogue, *Bulletin of Volcanology*, *77*(10), 89, doi:10.1007/s00445-015-0973-4.

Fenwick, D., C. Scheidt, and J. Caers (2014), Quantifying Asymmetric Parameter Interactions in Sensitivity Analysis: Application to Reservoir Modeling, *Mathematical Geosciences*, *46*(4), 493–511, doi:10.1007/s11004-014-9530-5.

Ferziger, J. H., and M. Peric (2002), *Computational Methods for Fluid Dynamics*, 3rd ed., 426 pp., Springer-Verlag, New York.

Gaunt, H. E., P. R. Sammonds, P. G. Meredith, R. Smith, and J. S. Pallister (2014), Pathways for degassing during the lava dome eruption of Mount St. Helens 2004-2008, *Geology*, *42*(11), 947–950, doi:10.1130/G35940.1.

Gerlach, B. T. M., K. A. Mcgee, and M. P. Doukas (2008), Emission Rates of CO2, SO2, and H2S, Scrubbing, and Preeruption Excess Volatiles at Mount St. Helens, 2004-2005, *A Volcano Rekindled: The Renewed Eruption of Mount St. Helens 2004-2006, U.S. Geological Survey Professional Paper 1750*, pp. 543–571.

Gonnermann, H. M., and M. Manga (2007), The Fluid Mechanics Inside a Volcano, *Annual Review of Fluid Mechanics*, *39*, 321–356, doi: 10.1146/annurev.fluid.39.050905.110207.

Gonnermann, H. M., and M. Manga (2013), Dynamics of magma ascent in the volcanic conduit, in *Modelling Volcanic Processes: The Physics and Mathematics of Volcanism*, edited by S. Fagents, T. Gregg, and R. Lopes, chap. 4, pp. 55–84, Cambridge University Press, Cambridge.

Hreinsdóttir, S., F. Sigmundsson, M. J. Roberts, H. Björnsson, R. Grapenthin, P. Arason, T. Árnadóttir, J. Hólmjárn, H. Geirsson, R. a. Bennett, M. T. Gudmundsson, B. Oddsson, B. G. Ófeigsson, T. Villemin, T. Jónsson, E. Sturkell, Ã. Höskuldsson, G. Larsen, T. Thordarson, and B. A. Óladóttir (2014), Volcanic plume height correlated with magma-pressure change at Grímsvötn Volcano, Iceland, *Nature Geosci.*, *7*(12), 214–218, doi:10.1038/ngeo2044.

Iverson, R. M. (2008), Dynamics of Seismogenic Volcanic Extrusion Resisted by a Solid Surface Plug, Mount St. Helens, 2004-2005, *A Volcano Rekindled: The Renewed Eruption of Mount St. Helens 2004-2006, U.S. Geological Survey Professional Paper 1750*, pp. 425–460.

Jaupart, C., and C. J. Allègre (1991), Gas content, eruption rate and instabilities of eruption regime in silicic volcanoes, *Earth and Planetary Science Letters*, *102*(3-4), 413–429, doi:10.1016/0012-821X(91)90032-D.

Kiser, E., I. Palomeras, A. Levander, C. Zelt, S. Harder, B. Schmandt, S. Hansen, K. Creager, and C. Ulberg (2016), Magma reservoirs from the upper crust to the Moho inferred from high-resolution Vp and Vs models beneath Mount St. Helens, Washington State, USA, *Geology*, *44*(6), G37,591.1, doi:10.1130/G37591.1.

Klug, C., and K. V. Cashman (1996), Permeability development in vesiculating magmas: implications for fragmentation, *Bulletin of Volcanology*, *58*, 87–100, doi: 10.1007/s004450050128.

Kozono, T., and T. Koyaguchi (2009), Effects of relative motion between gas and liquid on 1-dimensional steady flow in silicic volcanic conduits: 1. An analytical method, *Journal of Volcanology and Geothermal Research*, *180*(1), 21–36, doi:10.1016/j.jvolgeores.2008.11.006.

Kozono, T., and T. Koyaguchi (2012), Effects of gas escape and crystallization on the complexity of conduit flow dynamics during lava dome eruptions, *Journal of Geophysical Research: Solid Earth*, *117*(March), 1–18, doi:10.1029/2012JB009343.

Kozono, T., H. Ueda, T. Shimbori, and K. Fukui (2014), Correlation between magma chamber deflation and eruption cloud height during the 2011 Shinmoe-dake eruptions, *Earth, Planets and Space*, *66*(1), 139, doi:10.1186/s40623-014-0139-1.

Leonard, B. P. (1995), Order of accuracy of QUICK and related convection-diffusion schemes, *Applied Mathematical Modelling*, *19*(11), 640–653, doi:10.1016/0307-904X(95)00084-W.

Lisowski, M., D. Dzurisin, R. P. Denlinger, and E. Y. Iwatsubo (2008), Analysis of GPS-Measured Deformation Associated with the 2004-2006 Dome-Building Eruption of Mount St. Helens, Washington, *A Volcano Rekindled: The Renewed Eruption of Mount St. Helens 2004-2006, U.S. Geological Survey Professional Paper 1750*, pp. 301–333.

Liu, Y., Y. Zhang, and H. Behrens (2005), Solubility of H2O in rhyolitic melts at low pressures and a new empirical model for mixed H2O-CO2 solubility in rhyolitic melts, *Journal of Volcanology and Geothermal Research*, *143*(1-3), 219–235, doi: 10.1016/j.jvolgeores.2004.09.019.

Llewellin, E. W., and M. Manga (2005), Bubble suspension rheology and implications for conduit flow, *Journal of Volcanology and Geothermal Research*, *143*(1-3), 205–217, doi: 10.1016/j.jvolgeores.2004.09.018.

Manning, C. E., and S. E. Ingebritsen (1999), Permeability of the continental crust: Implications of geothermal data and metamorphic systems, *Reviews of Geophysics*, *37*(1), 127–150.

Mastin, L. G. (2002), Insights into volcanic conduit flow from an open-source numerical model, *Geochemistry, Geophysics, Geosystems*, *3*(7), 1–18.

Melnik, O., and R. Sparks (2006), Transient Models of Conduit Flows during Volcanic Eruptions, *Statistics in Volcanology (Special Publications of IAVCEI, No. 1)*, (2000), 201–214, doi:10.1144/IAVCEI001.16.

Melnik, O., and R. S. J. Sparks (2005), Controls on conduit magma flow dynamics during lava dome building eruptions, *Journal of Geophysical Research B: Solid Earth*, *110*(2), 1–21, doi:10.1029/2004JB003183.

Moran, S. C., S. D. Malone, a. I. Qamar, W. a. Thelen, a. K. Wright, and J. Caplan-Auerbach (2008), Seismicity Associated with Renewed Dome Building at Mount St. Helens, 2004-2005, *A Volcano Rekindled: The Renewed Eruption of Mount St. Helens 2004-2006, U.S. Geological Survey Professional Paper 1750*, pp. 27–60.

Neuberg, J. W., A. S. Collinson, P. A. Mothes, M. C. Ruiz, and S. Aguaiza (2018), Understanding cyclic seismicity and ground deformation patterns at volcanoes: Intriguing lessons from Tungurahua volcano, Ecuador, *Earth and Planetary Science Letters*, *482*, 193–200, doi:10.1016/j.epsl.2017.10.050.

Pallister, B. J. S., C. R. Thornber, K. V. Cashman, M. a. Clynne, H. a. Lowers, C. W. Mandeville, I. K. Brownfield, and G. P. Meeker (2008), Petrology of the 2004-2006 Mount St. Helens Lava Dome – Implications for Magmatic Plumbing and Eruption Triggering, *A Volcano Rekindled: The Renewed Eruption of Mount St. Helens 2004-2006, U.S. Geological Survey Professional Paper 1750*, pp. 647–702.

Papale, P. (2001), Dynamics of magma flow in volcanic conduits with variable fragmentation efficiency and nonequilibrium pumice degassing, *Journal of Geophysical Research: Solid Earth*, *106*(B6), 11,043–11,065, doi:10.1029/2000JB900428.

Park, J., G. Yang, A. Satija, C. Scheidt, and J. Caers (2016), DGSA: A Matlab toolbox for distance-based generalized sensitivity analysis of geoscientific computer experiments, *Computers and Geosciences*, *97*, 15–29, doi:10.1016/j.cageo.2016.08.021.

Rice, J. R., N. Lapusta, and K. Ranjith (2001), Rate and state dependent friction and the stability of sliding between elastically deformable solids, *Journal of the Mechanics and Physics of Solids*, *49*(9), 1865–1898, doi:10.1016/S0022-5096(01)00042-4.

Rust, A. C., and K. V. Cashman (2004), Permeability of vesicular silicic magma: Inertial and hysteresis effects, *Earth and Planetary Science Letters*, *228*(1-2), 93–107, doi: 10.1016/j.epsl.2004.09.025.

Saar, M. O., and M. Manga (1999), Permeability-porosity relationship in vesicular basalts, *Geophysical Research Letters*, *26*(1), 111–114, doi:10.1029/1998GL900256.

Saballos, J. A., V. Conde, R. Malservisi, C. B. Connor, J. Álvarez, and A. Muñoz (2014), Relatively short-term correlation among deformation, degassing, and seismicity: A case study from Concepción volcano, Nicaragua, *Bulletin of Volcanology*, *76*(8), 1–11, doi: 10.1007/s00445-014-0843-5.

Salari, K., and P. Knupp (2000), Code Verification by the Method of Manufactured Solutions, *Tech. rep.*, Sandia National Laboratories, Albuquerque, New Mexico.

Schilling, S. P., R. Thompson, J. Messerich, and E. Y. Iwatsubo (2008), Use of Digital Aerophotogrammetry to Determine Rates of Lava Dome Growth, Mount St. Helens, Washington, 2004-2005, *A Volcano Rekindled: The Renewed Eruption of Mount St. He-*

lens 2004-2006, U.S. Geological Survey Professional Paper 1750, pp. 145–167.

Schneider, A., A. W. Rempel, and K. V. Cashman (2012), Conduit degassing and thermal controls on eruption styles at Mount St. Helens, *Earth and Planetary Science Letters*, *357-358*, 347–354, doi:10.1016/j.epsl.2012.09.045.

Scott, W. E., D. R. Sherrod, and C. A. Gardner (2008), Overview of the 2004 to 2006, and Continuing, Eruption of Mount St. Helens, Washington, *A Volcano Rekindled: The Renewed Eruption of Mount St. Helens, 2004-2006: US Geological Survey Professional Paper 1750*, (October 2004), 3–22.

Segall, P. (2013), Volcano deformation and eruption forecasting, *Geological Society, London, Special Publications*, *380*, 85–106, doi:10.1144/SP380.4.

Slezin, Y. (2003), The mechanism of volcanic eruptions (a steady state approach), *Journal of Volcanology and Geothermal Research*, *122*(1-2), 7–50, doi:10.1016/S0377-0273(02)00464-X.

Smith, R., P. R. Sammonds, H. Tuffen, and P. G. Meredith (2011), Evolution of the mechanics of the 2004-2008 Mt. St. Helens lava dome with time and temperature, *Earth and Planetary Science Letters*, *307*(1-2), 191–200, doi:10.1016/j.epsl.2011.04.044.

Vallance, J., D. Schneider, and S. Schilling (2008), Growth of the 2004-2006 Lava-Dome Complex at Mount St. Helens, Washington, *A Volcano Rekindled: The Renewed Eruption of Mount St. Helens 2004-2006, U.S. Geological Survey Professional Paper 1750*, pp. 169–208.

Whittington, A. G., B. M. Hellwig, H. Behrens, B. Joachim, A. Stechern, and F. Vetere (2009), The viscosity of hydrous dacitic liquids: Implications for the rheology of evolving silicic magmas, *Bulletin of Volcanology*, *71*(2), 185–199, doi:10.1007/s00445-008-0217-y.

Wong, Y.-q., P. Segall, A. Bradley, and K. Anderson (2017), Constraining the magmatic system at Mount St . Helens (2004-2008) using Bayesian inversion with physics-based models including gas escape and crystallization, *Journal of Geophysical Research: Solid Earth*, *122*, 1–29.

Yang, X.-M., P. M. Davis, and J. H. Dieterich (1988), Deformation from inflation of a dipping finite prolate spheroid in an elastic half-space as a model for volcanic stressing, *Journal of Geophysical Research*, *93*(B5), 4249, doi:10.1029/JB093iB05p04249.